AMERICAN
METEOROLOGICAL
SOCIETY

Weather and Forecasting

EARLY ONLINE RELEASE

This is a preliminary PDF of the author-produced manuscript that has been peer-reviewed and accepted for publication. Since it is being posted so soon after acceptance, it has not yet been copyedited, formatted, or processed by AMS Publications. This preliminary version of the manuscript may be downloaded, distributed, and cited, but please be aware that there will be visual differences and possibly some content differences between this version and the final published version.

The DOI for this manuscript is doi: 10.1175/2011WAF2222455.1

The final published version of this manuscript will replace the preliminary version at the above DOI once it is available.

Improving Numerical Weather Predictions of Summertime Precipitation over the Southeastern U.S. through a High-Resolution Initialization of the Surface State

Jonathan L. Case[1*],

Sujay V. Kumar[2],

Jayanthi Srikishen[3], and

Gary J. Jedlovec[4]

[1]ENSCO Inc/Short-term Prediction Research and Transition (SPoRT) Center, Huntsville, AL

[2]SAIC/NASA Goddard Space Flight Center, Greenbelt, MD

[3]Universities Space Research Association (USRA), Huntsville, AL

[4]NASA Marshall Space Flight Center/SPoRT Center, Huntsville, AL

Revised manuscript submitted to *Weather and Forecasting*

January 2011

[*]*Corresponding Author Address*:
Jonathan L. Case, National Space Science and Technology Center, 320 Sparkman Dr., Room 3062, Huntsville, AL 35805. Email: Jonathan.Case-1@nasa.gov.

ABSTRACT

It is hypothesized that high-resolution, accurate representations of surface properties such as soil moisture and sea surface temperature are necessary to improve simulations of summertime pulse-type convective precipitation in high resolution models. This paper presents model verification results of a case study period from June–August 2008 over the Southeastern U.S. using the Weather Research and Forecasting numerical weather prediction model. Experimental simulations initialized with high-resolution land surface fields from the NASA Land Information System (LIS) and sea surface temperature (SST) derived from the Moderate Resolution Imaging Spectroradiometer (MODIS) are compared to a set of control simulations initialized with interpolated fields from the National Centers for Environmental Prediction 12-km North American Mesoscale model. The LIS land surface and MODIS SSTs provide a more detailed surface initialization at a resolution comparable to the 4-km model grid spacing. Soil moisture from the LIS spin-up run is shown to respond better to the extreme rainfall of Tropical Storm Fay in August 2008 over the Florida peninsula. The LIS has slightly lower errors and higher anomaly correlations in the top soil layer, but exhibits a stronger dry bias in the root zone. The model sensitivity to the alternative surface initial conditions is examined for a sample case, showing that the LIS/MODIS data substantially impact surface and boundary layer properties.

The Developmental Testbed Center's Meteorological Evaluation Tools package is employed to produce verification statistics, including traditional gridded precipitation verification and output statistics from the Method for Object-Based Diagnostic Evaluation (MODE) tool. The LIS/MODIS initialization is found to produce small improvements in the skill scores of 1-h accumulated precipitation during the forecast hours of the peak diurnal convective cycle. Because of very little union in time and space between the forecast and observed precipitation

systems, results from the MODE object verification are examined to relax the stringency of traditional grid point precipitation verification. The MODE results indicate that LIS/MODIS initialized model runs increase the 10 mm h^{-1} matched object areas ("hits") while simultaneously decreasing the unmatched object areas ("misses" plus "false alarms") during most of the peak convective forecast hours, with statistically significant improvements up to 5%. Simulated 1-h precipitation objects in the LIS/MODIS runs more closely resemble the observed objects, particularly at higher accumulation thresholds. Despite the small improvements, however, the overall low verification scores indicate that much uncertainty still exists in simulating the processes responsible for air-mass type convective precipitation systems in convection-allowing models.

1. Introduction

One of the most challenging weather forecast problems in the Southeastern U.S. is daily summertime pulse-type convection. Atmospheric flow and organized, synoptic-scale forcing are generally weak in this region during the summer. Thus, convection typically initiates in response to local low-level convergent boundaries such as sea/lake breezes, outflow boundaries, and other temperature and moisture discontinuities often related to horizontal gradients in surface heating rates. Numerical simulations of pulse-type convection usually have low skill, even in local predictions at high resolution, due to the inherent chaotic nature of these precipitation systems. Forecast errors can arise from assumptions within physics parameterizations, model resolution limitations, and uncertainties in initial atmospheric state and land surface properties. For this study, it is hypothesized that high-resolution, accurate representations of surface properties such as soil moisture, soil temperature, and sea surface temperature (SST) are necessary to better simulate the interactions between the surface and atmosphere, and ultimately improve predictions of local circulations and summertime pulse-type convection.

The impact of soil moisture heterogeneity and land surface (and ocean) properties on surface fluxes, boundary layer properties, and warm-season quantitative precipitation forecasts continues to be an important topic. On the large scale, Koster et al. (2000) showed that SSTs contribute to precipitation predictability in the Tropics while soil moisture states contribute to precipitation predictability in transition zones between dry and humid climate regions. Koster and Suarez (2003) demonstrated that the land surface initialization has a statistically significant impact on summer precipitation in continental regions that experience large soil moisture anomalies, and strong sensitivities of evaporation to soil moisture and precipitation to evaporation. Koster et al. (2004) ran retrospective atmospheric general circulation model simulations initialized with

realistic land surface model (LSM) fields to show the importance of a proper land surface initialization on the forecast skill of summer precipitation over the North American Great Plains.

Soil moisture heterogeneity can lead to the development of mesoscale circulations nearly as strong as sea-breeze circulations (Ookouchi et al. 1984; Avissar and Pielke 1989). These mesoscale circulations and associated heat fluxes are affected by large-scale winds, the distribution of soil wetness, and the wavelength of the land-surface discontinuities (Chen and Avissar 1994a), and can significantly affect the development and intensity of clouds and precipitation (Chen and Avissar 1994b). Chen and Dudhia (2001) highlighted the importance of improving the model soil moisture initialization at fine scales due to the sensitivity of soil thermal properties, hydraulic conductivity, and the surface energy budget on variations in soil moisture. A positive feedback mechanism between soil moisture and precipitation was presented in Eltahir (1998), in which the author described how wet soil moisture conditions lead to an increase in net solar and terrestrial radiation, and atmospheric water vapor that are concentrated in a shallower boundary layer, resulting in greater moist static energy per unit mass favoring convective rainfall processes. These positive feedbacks between soil moisture and convective precipitation likely occur during the summer months over much of the eastern U.S. (Findell and Eltahir 2003). Trier et al. (2004) examined a case of convective initiation along a dryline in which the numerical simulations were quite sensitive to the initial soil moisture details, which led to localized differences in the sensible and latent heat fluxes and corresponding low-level thermodynamic structure.

The International H2O Project 2002 field campaign (IHOP_2002) took place over the U.S. Southern Great Plains during the late Spring and early Summer of 2002 with some of its primary goals to improve convective initiation predictions and quantitative precipitation forecasts in

numerical weather prediction models (Weckworth et al. 2004; Weckworth and Parsons 2006). The land surface component of IHOP_2002 included a sophisticated observational network to measure land surface variables in order to examine the effects of surface properties on boundary layer evolution, evaluate LSMs, and assess the role of LSMs in improving numerical convective forecasts (LeMone et al. 2007). LeMone et al. (2008) evaluated characteristics of the Noah LSM for a fair-weather case during IHOP_2002 while Holt et al. (2006) modeled a convective initiation case study, initializing the land surface with an offline version of the Noah LSM. Holt et al. (2006) found that synoptically-driven convection along a dryline tended to be delayed in its onset relative to observations in all their sensitivity runs; however, the inclusion of a sophisticated transpiration model resulted in more skillful air temperature and moisture forecasts. Also, Trier et al. (2008) documented that the choice of LSM and initial soil moisture distribution both had major impacts on the evolving thermodynamic variables in the PBL and subsequent precipitation forecasts in a convection-allowing model configuration.

Numerical models have been shown to be sensitive to the input land and ocean surface initialization data in the southeastern U.S. as well. Baker et al. (2001) found through idealized simulations over central Florida that soil moisture initialization impacted the timing and location of precipitation, with areas of wet soils preferentially focusing heavy precipitation. Case et al. (2008) presented improvements to simulated sea breezes and surface verification statistics over Florida by initializing the Weather Research and Forecasting (WRF) numerical weather prediction model with land surface variables from an offline spin-up run of the NASA Land Information System (LIS). LaCasse et al. (2008) documented the sensitivity of WRF model simulations over oceanic regions around Florida to high-resolution SSTs derived from the Moderate Resolution Imaging Spectroradiometer (MODIS) aboard NASA's polar orbiting Aqua

and Terra satellites. The authors found that the static stability near the Florida East Coast decreased under easterly flow regimes, and that favored zones of low-level convergence occurred near Florida's East Coast under easterly flow and over the Florida Current under westerly flow.

Many of these studies have highlighted the challenges involved in quantifying the impact of the land surface condition on PBL evolution and convection. To this end, community-wide efforts to converge on metrics of land-atmosphere interactions (e.g. 'coupling strength') include those at global (GLACE; Koster et al. 2006) and local (LoCo; Santanello et al. 2009) scales. A missing component of these community-wide studies has been a rigorous evaluation of the actual impacts of high-resolution land representation in a forecast environment and on sensible weather.

With these issues in mind, this paper focuses on the impacts of a subset of high-resolution surface initialization datasets on numerical model simulations of typical pulse-type, summertime convection over a southeastern U.S domain, with an emphasis on precipitation verification. One of the added challenges to this study is that during the summer, the southeastern U.S. does not typically experience well-organized synoptic-scale forcing (e.g. fronts and drylines) such as that previously studied over the U.S Great Plains during campaigns like IHOP_2002. In particular, the impact of soil moisture on precipitation should be most clearly identifiable for locally-coupled and weak synoptic forcing conditions such as in this experiment.

This modeling study makes use of both the NASA LIS for land surface initialization and 2-km resolution MODIS SSTs for ocean initialization to examine the sensitivity to and possible improvements realized from these datasets. Both traditional and object-based precipitation verification results are highlighted. The remainder of this paper is organized as follows. Section 2 provides a description of the surface initialization datasets for the model simulations. Section 3

describes the simulation methodology for the sensitivity experiment. Results are presented in Section 4, and conclusions are given in Section 5.

2. Surface Initialization Datasets

High-resolution surface datasets are generated for both the land and ocean surface in order to provide detailed information physically consistent with the WRF model resolution of this study. A brief description of each dataset is given below.

a. NASA Land Information System

The NASA LIS is a high performance land surface modeling and data assimilation system that integrates satellite-derived datasets, ground-based observations and model reanalyses to force a variety of LSMs (Kumar et al. 2006, 2007). By using scalable, high-performance computing and data management technologies, LIS can run LSMs offline globally with a grid spacing as fine as 1 km to characterize land surface states and fluxes.

To provide physically-consistent land surface initialization data in a simulated real-time environment, the Noah LSM (Ek et al. 2003) is run offline (i.e. uncoupled) within LIS at the same horizontal grid spacing as the WRF grid. The goal here is to demonstrate a realistic scenario in which a generalized LIS initialization dataset could be provided to a variety of users (e.g. National Weather Service forecast offices and other government, university, and private sector weather entities) running their own local modeling application on domains with comparable grid resolution.

For consistency, the Noah LSM in the offline LIS uses the same soil and vegetation database as in the WRF model. The soil properties are represented by the State Soil Geographic (STATSGO; Miller and White 1998) database. For the land-water mask and land cover type, the

U.S. Geological Survey 1-km global database derived from the Advanced Very High Resolution Radiometer (AVHRR) satellite data from 1992–1993 is up-scaled to the WRF grid resolution. Additional required parameters include quarterly climatologies of albedo (Briegleb et al. 1986) and maximum snow surface albedo (Robinson and Kukla 1985), monthly climatologies of greenness vegetation fraction data derived from AVHRR with a native resolution of ~14 km (Gutman and Ignatov 1998), and a deep soil temperature climatology (serving as a lower boundary condition for the soil layers) at 3 meters below ground, derived from 6 years of Global Data Analysis System (GDAS) 3-hourly averaged 2-m air temperatures using the method described in Chen and Dudhia (2001).

The offline LIS run is cold-started on 1 January 2004 with a uniform first-guess soil temperature and volumetric soil moisture of 290 K and 25%, respectively, in all soil layers. The Noah LSM is integrated for a time period of 4 years, 5 months from 1 January 2004 to 1 June 2008, using a time step of 30 minutes. Such a long integration time is used to ensure that the model states can reach a fine-scale equilibrium with the forcing meteorology (Cosgrove et al. 2003b; Rodell et al. 2005). Atmospheric input to the LIS/Noah run is provided by GDAS analyses (Derber et al. 1991), which consists of three-hourly data at a horizontal resolution of 0.469° (~52 km). Precipitation forcing from the Stage IV high-resolution analyses replace the GDAS precipitation, providing a detailed antecedent precipitation field. The Stage IV product consists of hourly ~5-km precipitation analyses produced operationally by the U.S. River Forecast Centers, based on rain gauges and radar precipitation estimates from the Weather Surveillance Radar-1988 Doppler network (Lin and Mitchell 2005; Lin et al. 2005). The forcing fields are downscaled to the running resolution within LIS using bilinear or conservative (for precipitation) interpolation approaches. In the case of downward shortwave radiation, an

additional zenith-angle based temporal disaggregation is applied (Cosgrove et al. 2003a). The forcing fields of downward-directed longwave radiation, pressure, 2-m air temperature and 2-m relative humidity are further topographically corrected via lapse-rate and hypsometric adjustments using the elevation data differences between the LIS and native GDAS forcing grid (Cosgrove et al. 2003a).

b. MODIS Sea Surface Temperatures

MODIS SST gridded composites, produced by the NASA Short-term Prediction Research and Transition (SPoRT; Goodman et al. 2004) Center, are created at 2-km resolution by combining data from multiple passes of the polar-orbiting Earth Observing System satellites (Haines et al. 2007). The compositing technique assumes that the day-to-day variation of SST is relatively small — the degree to which this assumption is valid will likely vary spatially and seasonally. Data from both the Terra and Aqua platforms are combined to create separate day/night composites for a total of four composites per day valid at 0400, 0700, 1600, and 1900 UTC. Care is taken to remove most cloud contamination in the Haines et al. (2007) compositing technique. A binary cloud mask is first applied prior to computing the SST at a given pixel. Next, the warmest two of the most recent three SST values in the collection for each pixel are averaged, thereby discarding the coldest reading and removing possible cloud-contaminated pixels that may have eluded detection by the cloud mask.

3. Experiment Design

A modeling sensitivity experiment is conducted with version 3.0.1.1 of the Advanced Research WRF (ARW; Skamarock et al. 2008) in which the land and ocean/lake surface data from the National Centers for Environmental Prediction (NCEP) North American Mesoscale (NAM) model are replaced with high-resolution data from a LIS offline simulation and MODIS

SST composites, respectively. Details on the specific model configurations, initialization datasets, and verification methodologies are described below.

a. Model Configuration and Period of Study

This investigation consists of a set of control and experimental ARW simulations initialized once per day at 0300 UTC from June to August 2008. This initialization time is chosen to mimic the local model configurations used by the NOAA/NWS Miami, FL and Mobile, AL. The combination of limited computational resources, a need for timely model output, and the use of local atmospheric analyses for initializing the atmosphere at these offices (i.e. the Local Analysis and Prediction System) justifies the choice of an "off-hour" initialization time. A total of 81 paired control and experimental forecasts are generated, with a few days unavailable due to missing MODIS SST composites. The model is integrated 27 hours to 0600 UTC the following day, similar to the operational runs made at NOAA/NWS Miami, FL and Mobile, AL. The simulation domain consists of a single grid of 309 x 311 staggered points in the zonal and meridional directions, respectively, at 4-km horizontal grid spacing, centered over the Southeastern United States. The grid contains 39 sigma-pressure vertical levels extending from the surface to a domain top of 50 mb. The vertical spacing is stretched from a minimum of 0.004 sigma near the surface (corresponding to ~40 m) to a maximum of 0.034 sigma at upper levels.

The model physics schemes are chosen to emulate the real-time configuration of the 4-km ARW at the National Severe Storms Laboratory, which focuses especially on convection and severe weather forecasting problems (Kain et al. 2010). For both the control and LIS+MODIS-initialized simulations (hereafter LISMOD), the ARW physics options consist of the rapid radiative transfer model (Mlawer et al. 1997) and the Dudhia scheme (Dudhia 1989) for longwave and shortwave radiation, respectively. The WRF Single Moment 6-class microphysics

scheme (WSM6, Hong and Lim 2006; Skamarock et al. 2008) is used without any convective parameterization physics; thus, all convection is determined explicitly by the WSM6 microphysics and model dynamics. The planetary boundary layer and turbulence processes are parameterized by the Mellor-Yamada-Janjić scheme (Janjić 1990, 1996, 2002). Horizontal diffusion is handled by the two-dimensional Smagorinsky first-order closure scheme (Smagorinsky et al. 1965). All runs use the Noah LSM as configured in version 3.0.1.1 of the ARW, being nearly identical to the version run operationally at NCEP (Chen and Dudhia 2001; Skamarock et al. 2008; Ek et al. 2003). Surface-layer calculations of friction velocities and exchange coefficients needed for the determination of sensible and latent fluxes in the LSM are provided by the NCEP Eta similarity theory scheme (Janjić 1996, 2002). The positive-definite advection options for moisture and scalars are enabled to remove the possible unphysical effects and high precipitation bias that can result from the "clipping" of negative mixing ratios in the 3rd order Runge-Kutta transport scheme (Skamarock and Weisman 2008; Skamarock et al. 2008).

For the control runs, all initial conditions for the atmosphere, land, and the NCEP Real-Time Global (RTG) SSTs come from the native-resolution (12-km, grib 218) NCEP NAM model 3-h forecast initialized at 0000 UTC. Three-hourly boundary conditions for both the control and LISMOD runs are provided by the NAM model 3-h to 30-h forecasts. The SSTs remain fixed throughout the 27-h ARW simulations. Interpolation of initial and boundary condition data is done with the WRF Pre-Processing System (WPS) utilities.

b. Experimental Simulations

The experimental runs are identical to the control configuration except that the land surface initial conditions are replaced by output from the offline LIS spin-up run and the RTG SSTs of the NAM model are replaced by the 2-km MODIS SST composites. The LIS data are output in

GRIB1 format daily at 0300 UTC for the period of record (June – August 2008) to initialize the WRF land surface fields in the LISMOD simulations. The GRIB1 formatted LIS data are used by the WPS with only a few minor modifications required. First, the WPS file "METGRID.TBL" is modified to handle the LIS land-sea mask for interpolation of data to the WRF grid. The new LIS land-sea mask defined in METGRID.TBL is then applied to each of the land surface variables to be interpolated to the WRF grid. In addition, the interpolation method used in WPS for the LIS fields is a nearest-neighbor approach, as this method preserves the most detail and minimizes differences caused by interpolation. A summary of all the LIS fields incorporated into the WRF initial conditions is given in Table 1.

The MODIS SST composite from 0400 UTC the previous day is incorporated into the daily WRF initial conditions at 0300 UTC to minimize diurnal variations in SST relative to the model initialization time. The only exception occurs for model initializations from 3–14 June 2008, when SST data are missing for the 0400 UTC MODIS composites. For these initializations, the 0700 UTC MODIS composites from the previous day provide the SST initial conditions. For all simulations, the SSTs are held fixed throughout the duration of the forecast. This approach may not be the most realistic, since SST does have a low amplitude diurnal cycle under clear sky / calm wind conditions (Zeng and Beljaars 2005); however, we attempt to show the value of the more accurate, higher spatial resolution SST data on the forecast fields.

c. Verification Methodology and Tools

For verifying precipitation and other fields in both the control and LISMOD runs, the Meteorological Evaluation Tools (MET) package is employed (Brown et al. 2009). Created by the WRF Developmental Testbed Center at the National Center for Atmospheric Research, the MET package is a highly-configurable, state-of-the-art suite of model verification tools. Both

traditional statistics and the object-oriented verification methodology available in MET are applied. Known as the Method for Object-based Diagnostic Evaluation (MODE; Brown et al. 2007; Davis et al. 2009), this utility classifies "objects" in gridded fields, calculates a wide variety of object attributes, and merges/pairs forecast objects with observed objects to determine the similarities and differences between the various objects. This utility is used to obtain more meaningful precipitation verification statistics of pulse-type convection over the southeastern U.S., compared to traditional grid-point by grid-point verification techniques.

4. Results

This section provides results that illustrate some of the differences between the LIS land surface and MODIS SST initialization versus the interpolated NAM data in the control runs. Sample forecast impacts are presented, as well as verification output from MET/MODE.

a. LIS Offline Run Results from Tropical Storm Fay

A high-impact event that affected the domain during the period of record is Tropical Storm Fay in late August. In the 8-day period from 18–26 August, the storm produced prodigious amounts of rainfall across eastern and northern Florida, southwestern Georgia, and Alabama, with some local maxima exceeding 700 mm. Needless to say, the volumetric soil moisture increased dramatically during this 8-day period over the affected areas. The root zone layer in the Noah LSM (40–100 cm) should have a substantial impact on the subsequent evapo-transpiration into the atmosphere. Figure 1 depicts the moistening of the 40–100 cm soil layer from 18–26 August, comparing changes in the Control/NAM initialization (panel a) to the LIS initialization (panel b). Both model initialization differences show a similar broad pattern of moistening from Florida and southern Georgia into east-central Mississippi that follows the general pattern of rainfall depicted in Figure 1c. The LIS differences have much more detail as

expected; however, the LIS (Figure 1b) has substantially higher amounts of moistening across much of the eastern Florida peninsula, which visually corresponds much better to the pattern of the rainfall maximum in Figure 1c compared to the Control (Figure 1a).

A LIS/Noah time-depth cross section at a selected point in southwestern Georgia (Figure 1d) helps to illustrate the dramatic soil moistening associated with Tropical Storm Fay. At this location, the soil type is categorized as "loamy sand", which has wilting/porosity points of 3% and 42%, respectively. In about a day, the volumetric soil moisture in the upper one meter increases from a minimum of less than 6% to a maximum value near 40%, transitioning from near the wilting point to porosity. Such a sudden shift from excessively dry to moist can have substantial impacts on the surface energy budget and subsequent short-term forecasting issues. It is therefore important to be able to capture accurately the rapid changes to the soil moisture field in such situations in order to improve subsequent short-term numerical simulations.

b. Differences in Surface Initialization Datasets

The combination of LIS spin-up data and MODIS SSTs provide a more detailed representation of the land and water surface compared to the control run using interpolated 12-km NAM data. The depiction of 0–10 cm soil moisture at 0300 UTC 9 June 2008 in Figure 2 helps to illustrate this point. While the regional patterns of soil moisture are fairly similar, the LISMOD initialization data provides information more consistent with the resolution of the WRF model in Figure 2b. Locally more moist conditions are resolved in LIS within the narrow river valleys of eastern Georgia and South Carolina, where soil textures containing a higher silt content retain more moisture compared to the surrounding sandy soils. The difference field also indicates systematically drier initial conditions in this soil layer from southern Mississippi to northwestern South Carolina (Figure 2c). Over Florida, drier soil moisture is interspersed with

local pockets of wetter soil moisture. These soil moisture variations are likely attributed to differences between the 12-km NAM Data Assimilation System (NDAS), which front-ends the NAM model, and the GDAS, which forces the LIS off-line run in combination with the Stage-IV precipitation analyses. Also, the ability of the 4-km LIS to better capture local areas of antecedent convective-type precipitation compared to the 12-km NDAS explains the local variations in soil moisture over Florida. It should be noted that the NDAS also uses the Stage-IV precipitation product to initialize its soil fields, similar to the offline LIS run.

A validation of the LIS versus control (NAM) soil moisture is conducted at available observation sites from the U.S. Department of Agriculture's Soil Climate Analysis Network (SCAN, Schaefer et al. 2007). Twenty-eight available SCAN observation sites fall within the WRF modeling domain, but most sites are clustered in northern Alabama and western Mississippi (Figure 3). SCAN measures soil temperature and volumetric soil moisture at depths of 2, 4, 8, 20, and 40 inches (~5, 10, 20, 50, and 100 cm) at most locations.

There is an inherent ambiguity that occurs with directly comparing a soil moisture or temperature in a grid box to an observation at a point, primarily due to spatial heterogeneities in soil type and vegetation coverage (Robock et al. 2003; Marshall et al. 2003; Godfrey and Stensrud 2008). Therefore, the soil temperature and moisture in the model initial conditions are evaluated using a spatial averaging technique similar to that presented in Robock et al. (2003) and Godfrey and Stensrud (2008). In addition, a depth-weighted average of the root zone is computed in a manner following Reichle et al. (2007) and soil moisture anomaly correlations are calculated similar to Kumar et al. (2009).

The modeled near-surface soil moisture and temperature in the 0–10 cm layer are directly compared to SCAN observations at 5 cm, representing the mid-point of this layer. For the

modeled soil moisture and temperature in the root zone, a depth-weighted average of the 10–40 cm and 40–100 cm layers is computed as follows:

$$Fcst_{RZ} = \frac{30(Fcst_{10\text{-}40\text{cm}}) + 60(Fcst_{40-100\,cm})}{90}. \quad (1)$$

The depth-weighted observed soil moisture and temperature in the root zone is determined by:

$$Obs_{RZ} = \frac{5(Obs_{10cm}) + 10(Obs_{20\,cm}) + 25(Obs_{50cm}) + 50(Obs_{100\,cm})}{90}. \quad (2)$$

At each model initialization hour (0300 UTC), the spatial average of the modeled control and LISMOD soil moisture and temperature interpolated to the SCAN locations is computed along with the spatial average of the observed soil moisture and temperature.

The results indicate that both the control/NAM and LIS soil moisture initializations more closely emulate the observations and trends at 5 cm than in the root zone. Figure 4a shows that day-to-day variations in modeled 5-cm soil moistures trend similarly to the observations, with the LIS tending to be closer to the observations, especially in June and July. However, both of the modeled soil moisture time series experience a sluggish response to precipitation events relative to the observations, consistent with the findings in Marshall et al. (2003) and Godfrey and Stensrud (2008). The anomalies in the control/NAM and LIS are very similar during the period of record (Figure 4b). In the root zone, both the NAM and LIS have considerably drier soil moisture than the SCAN observations throughout the entire summer, with the LIS being drier than the NAM by about 2–3% (Figure 4c). This dry bias in the root zone is also consistent with the results in Godfrey and Stensrud (2008). The anomalies in the root zone trend nearly identically between the NAM and LIS in which both model initializations have too much amplitude about the summer mean compared to the root zone SCAN observations (Figure 4d).

The anomaly correlations of the spatial averaged soil moisture are nearly identical at both 5 cm (0.875 for NAM; 0.871 for LIS) and the root zone (0.549 for NAM; 0.561 for LIS).

The differences between the NAM and LIS are even smaller when examining the spatial averages of the soil temperature. Again, both the modeled soil temperatures are more similar to the observations at 5 cm than in the root zone (Figure 5). Both the NAM and LIS have root zone temperatures consistently cooler than the SCAN observations by about 2–3 K (Figure 5b). Interestingly, the 5-cm soil temperatures exhibit a slightly greater range than the observed 5-cm soil temperatures, despite the fact that the 5-cm modeled soil moisture was generally too moist during June and July. Further investigation is needed to determine the source of this inconsistency, which could be related to an improper representation of the soil characteristics, soil heat flux, and/or incoming energy from the atmospheric forcing dataset. The similar behavior between the NAM and LIS presented in these figures suggests that the biases being realized (particularly in the root zone) may be a manifestation of the Noah land surface model physics and/or mis-classification of the land surface properties, since the Noah model and same fixed parameters are used in both the NAM and the LIS for this experiment.

Despite the ambiguities between modeled and point observations of soil variables, the validation statistics at the individual SCAN stations are also examined, since a goal of this study is to determine the impacts of introducing spatial variability in the surface initialization that is more consistent with the model grid resolution. Table 2 summarizes the bias, RMS error and anomaly correlation statistics at the individual SCAN stations. The results are generally consistent with the spatial averaged statistics in that the LIS is slightly drier than the NAM soil moisture as indicate by a decrease in the bias of 1–2%. The LIS 5-cm soil moisture has a higher anomaly correlation of 0.722 compared to the NAM model's 0.657. The root zone anomaly

correlations are nearly identical to one another. The soil temperature evaluated at the individual stations indicates roughly a 0.2 K increase in the RMS error in the LIS initial conditions. Anomaly correlations are quite similar with the NAM slightly higher than the LIS at both the 5-cm level and root zone layer.

From a verification perspective, the mixed results make it difficult to determine which soil initial field is consistently more accurate, especially considering the sparseness and variable density of the SCAN observations. The results do suggest that LIS is perhaps providing a better initial conditions of the upper soil layer (5 cm) as a result of the Noah LSM spin-up with Stage IV precipitation analyses on a higher resolution grid compared to the NAM 12-km resolution. The main points we can conclude are that the LIS produced a slightly drier overall soil layer compared to the NAM (at least at the SCAN locations), and that the 4-km LIS provided greater horizontal detail, which is probably more representative at 5cm given the modest improvement in the LIS soil moisture anomaly correlation.

Meanwhile over the adjacent waters, the MODIS SST product provides much more thermal structure over the Gulf of Mexico and Atlantic waters compared to the interpolated RTG SSTs from the NAM model (Figure 6). For the model run initialized at 0300 UTC 9 June, SSTs were obtained from the 0700 UTC 8 June SPoRT/MODIS composite. Substantial differences (up to 2°C) are found in the vicinity of the shallow near-coastal waters near the Florida coast. For this composite, the MODIS tends to be cooler than the RTG. However, many days in late July and August have patterns of both warming and cooling relative to the RTG SSTs (not shown).

The most noteworthy aspect of the MODIS composite is its ability to capture the fine-scale horizontal gradients in SSTs compared to the once-daily RTG product. The smoothness of the RTG data in Figure 6a precludes the model from capturing the relatively cool shelf waters off the

Florida East Coast. However, the LISMOD SSTs in Figure 6b are able to depict the cool shelf waters and the magnitude of the Gulf Stream east of Florida. The SST differences illustrate the locally sharper horizontal gradients captured by the SPoRT MODIS product in Figure 6c. Previous studies have documented improved error statistics of the SPoRT MODIS product compared to RTG SSTs (Haines et al. 2007) and the positive benefit realized in numerical simulations (LaCasse et al. 2008).

c. Sample Forecast Sensitivities from 9 June

The surface initialization differences depicted in Figure 2 and Figure 6 lead to distinct impacts on the model predicted thermodynamic properties (Figure 7). The corridor of drier LIS soil moisture from southern Mississippi to northwestern South Carolina results in an increase of sensible heat flux by over 50 W m^{-2} in many locations at the 13-h forecast valid at 1600 UTC 9 June (Figure 7a). The partitioning of higher sensible heat flux relative to the latent heat flux produces a decrease in the simulated 2-m dew point temperature by as much as 2°C across this corridor (Figure 7b). The increased surface heating also produces locally higher PBL heights (Figure 7c), especially over southwestern Mississippi and central Georgia. The combination of a decrease in the moisture transport into a deepening boundary layer subsequently results in smaller values of convective available potential energy (CAPE) particularly over portions of southern Mississippi, northeastern Louisiana, central Georgia and northwestern South Carolina. Parts of west-central Georgia experience CAPE reductions of 500 J kg^{-1} or more. These results are consistent with the dry soil corollary of the feedback mechanism described in Eltahir (1998).

The impacts from the LIS soil initialization is far more complicated over the Florida peninsula. The detailed variations in the LIS soil moisture relative to the control/NAM produce local pockets of alternating higher/lower sensible heat flux (Figure 7a), likely related to

antecedent rainfall from the Stage IV precipitation forcing in the LIS spin-up. The propensity is for higher sensible heat fluxes and lower 2-m dew point temperatures across the Florida peninsula, ultimately resulting in a greater coverage of lower CAPE (Figure 7d). Interestingly over the Gulf of Mexico, the CAPE tends in *increase* despite a slight cooling of the SSTs from the MODIS composite in the 9 June model initialization. This scenario is likely a manifestation of the decrease in the PBL height (Figure 7c) helping to concentrate the moisture transport from the ocean surface into a shallower boundary layer. These substantial modifications to the heat fluxes and CAPE certainly have the potential to impact convective rainfall in the model.

A sample 1-h forecast precipitation comparison ending 2100 UTC 9 June 2008 is presented in Figure 8. The flow pattern was very weak on this day, with few discernable boundaries or organized flow pattern over the southeastern U.S. Figure 8 shows how the forecast 1-h precipitation patterns and modes are quite similar overall in the control and LISMOD runs. However, the difference field depicts numerous small-scale fluctuations between the forecasts (Figure 8c). Compared to the Stage-IV product in Figure 8d, both simulations over-predict precipitation across northern Mississippi and Alabama while under-predicting rainfall over the southern portions of these states. Both the control and LISMOD runs appear to be most skillful in predicting the convection over the western part of the Florida peninsula.

At first glance, the precipitation forecast sensitivities appear somewhat subtle, despite relatively substantial changes in the details of the land and water initial conditions. A qualitative examination of many different days during the period of record (not shown) indicated that the broad patterns of forecast precipitation in the control and LISMOD runs are generally similar, especially at longer accumulation intervals. The different model solutions tend to look more similar to one another rather than the validating Stage IV precipitation analysis, as is often the

case in high-resolution convection-allowing model runs under weak synoptic flow. Most of the differences in forecast precipitation arise from small-scale fluctuations in individual convective elements that evolve differently due to the variations in the land/water surface interactions with the PBL. If the control forecast is significantly in error with the timing and placement of precipitation, then the LISMOD is also generally in error. Therefore, it appears that the high-resolution input from LIS and MODIS SSTs leads to numerous small-scale variations in the convective precipitation pattern, while the broad-scale patterns of simulated precipitation are still largely driven by the atmospheric initial and boundary conditions, in addition to model dynamics and physics.

d. Selected Traditional Verification Statistics

Point verification statistics at approximately 500 primary and mesonet stations over the southeastern U.S. are calculated using the MET package. The bias and error standard deviation as a function of forecast hour (Figure 9a and b, respectively) for 2-m temperature and dew point temperature reveal relatively minor differences in most forecast hours. The bias plots (Figure 9a) indicate that the LISMOD develops a slightly higher warm bias by a few tenths of a degree Celsius between forecast hours 9 and 18, while a nominal dry dew point bias $\leq 0.5°C$ occurs between forecast hours 9 and 27. The error standard deviation in Figure 9b shows only small differences between control and LISMOD, with the LISMOD having marginally larger errors. Statistically significant results at the 95^{th} percentile are denoted by non-overlapping plots of the lower and upper confidence intervals on each series in Figure 9.

The 3-h NAM forecasts providing the initial conditions to both model runs experience a warm bias of nearly 2°C at 0 hours (Figure 9a). The temperature bias steadily decreases during the night into the daylight hours until 21 hours (0000 UTC), after which, the temperature bias

switches back to positive. A distinct diurnal signal is seen in the error standard deviation (representing the random errors) of the 2-m temperature and to a lesser extent the 2-m dew point temperature. Maximum random errors occur distinctly during the daytime between forecast hours 15 and 21 (1800 UTC to 0000 UTC, Figure 9b), and is likely attributed to the model's inability to forecast accurately the afternoon convection timing and location. False alarm convective outflow boundaries combined with forecast misses of actual outflow boundaries likely lead to the large random component of the errors during the afternoon and early evening hours, in both the temperature and dew point. These results are consistent with the findings in a previous model verification study over the Florida peninsula (Case et al. 2002).

Using traditional grid-point by grid-point techniques, the 1-h accumulated precipitation errors are computed during the forecast hours of typical peak convective activity (12–24 hours, corresponding to 1500–0300 UTC). The results indicate that both the control and LISMOD over-predict the area coverage of 1-h accumulated precipitation at all three thresholds examined (bias > 1 for 5-, 10-, and 25-mm h^{-1}; Figure 10a). However, the LISMOD tends to reduce the bias between forecast hours 12–18, especially at the higher intensities. The Heidke Skill Score in Figure 10b depicts a low skill under 0.10 for all precipitation thresholds, diminishing with forecast hour. The LISMOD has a marginally higher skill, mainly between forecast hours 12 and 18. Standard threat scores also reveal low skill for the 1-h accumulated precipitation, with the LISMOD being marginally higher at most forecast hours (Figure 10c). The 24-h accumulated precipitation statistics for the 3-h to 27-h forecasts show a similar story, with the LISMOD threat scores only marginally better than the control at each of the three thresholds (5 mm, 10 mm, and 25 mm, Figure 10d). The largest improvements in 24-h threat score occurs in the 25-mm threshold. All threat score changes in panels (c) and (d) are statistically significant where plots

of the lower and upper confidence intervals do not overlap. Overall, however, the traditional statistics differences are quite minor and do not reveal large performance differences in model accuracy, except for a reduction in the high-intensity precipitation bias resulting in slightly improved threat scores.

Because the model precipitation fields have so little overlap with the observed precipitation at most times, this measures-oriented approach to verification provides little utility for interpreting differences in the results. Many forecasters find value in high-resolution model precipitation forecasts based on the realism to observed features and depiction of the convective modes, despite the spatial and temporal biases and uncertainties that exist. Davis et al. (2006) describe the limitations of using traditional metrics in precipitation verification, as illustrated in Figure 1 of their paper, and present an object-based approach to precipitation verification applicable to higher-resolution model configurations.

To provide a better interpretation of the precipitation forecast differences in our high-resolution model forecasts, the MODE object-based technique in the MET verification package is invoked. Using the MODE tool enables a more lenient comparison between the simulated and observed precipitation similar to how a forecaster may interpret the quality of the forecast model. The MODE is tuned to identify detailed features at various accumulation thresholds, but does not require that the precipitation features exactly overlap to be considered a "hit".

e. MODE Object-Based Verification

The remainder of the analysis focuses on the non-traditional object-based verification available from MET's MODE tool. A snapshot of forecast/observed object pairs from the control and LISMOD simulation from 9 June is presented first, followed by overall composite results from running MODE over all 81 control and LISMOD forecasts from summer 2008.

The object-matching in MODE is centered on an "interest function", which combines several attributes about the feature of interest — in this case 1-h accumulated precipitation from the WRF model (forecast) and Stage IV precipitation analyses (observed). The attributes consist of object characteristics such as centroid distance, minimum boundary distance, orientation angle difference, etc. MODE resolves objects in a gridded field through convolution thresholding. This technique involves applying a filter function to the raw data using a tunable radius of influence. The filtered field is then thresholded using another tunable parameter (typically the precipitation threshold) to create a mask field. Finally, the raw data are restored to objects where the mask meets/exceeds the specified threshold. More information on the technical details of MODE can be gleaned from Brown et al. (2007) and Davis et al. (2009).

Forecast and observed objects are matched based on additional input criteria and a minimum value of the "interest function", which scales between 0 and 1. The fuzzy engine weights used to formulate the interest function are given in Table 3, and are simply the default values in the MET software. These weights seem reasonable for the problem at hand since they emphasize the distances between objects as the most important factors determining object similarity. Forecast/observed objects are considered matches if the interest function is ≥ 0.6 and the distance between the object centroids is no greater than 80 km. A single forecast object could be matched with more than one observed object and vice versa. The interest function is not calculated for object pairs whose centroids are greater than 80 km apart. The rationale for an 80-km restriction is to avoid having a precipitation object on the west coast of Florida be matched with one on the east coast of Florida, which should not be considered a "hit".

1) OUTPUT FROM 9 JUNE 2008

Output from MODE for precipitation objects of 10 mm or greater for the 1-h period ending 2100 UTC 9 June is given in Figure 11. A comparison between the control forecast and observed objects (Figure 11a, left column) shows one matched forecast precipitation object across southwest Florida with several false alarm objects across the western Florida peninsula. The LISMOD run (Figure 11b) has two matched 10-mm objects in southwestern Florida, a larger false alarm object over the west-central Florida peninsula and two very small false alarm objects in the interior part of the peninsula.

It should be noted that if we had increased the object centroid distance criterion (80 km), modified the fuzzy weights in Table 3, and/or relaxed the interest function threshold, then more forecast and observed objects would have been matched. Such a stringent requirement is used to minimize object matching for rainfall areas that a forecaster would not consider a "hit". Despite the somewhat stringent constraints placed on MODE, this configuration appears optimal based on the level of detail and accuracy desired for this experiment.

Once the object matching is done, the total area of matched and unmatched objects is provided at each forecast hour in the MODE output. A summary of the matched/unmatched objects areas for the 10 mm h^{-1} precipitation intensity (with forecast and observed object areas combined together) indicates that the LISMOD out-performed the control run on this day at many of the forecast hours (Table 4). Six of the 9 forecast periods experiencing 10 mm h^{-1} precipitation have reductions in the unmatched area in LISMOD, while 7 of 9 have increases in the total matched area. Meanwhile, the control has only 3 forecast periods with improvements in the unmatched area over LISMOD and no improvements in the matched area.

2) MODE VERIFICATION FOR SUMMER 2008

By applying the same object matching criteria to all forecasts for the summer 2008, we can determine whether the LISMOD consistently out-performed the control in 1-h precipitation forecasting accuracy during the peak convective hours. The analysis focuses on 10 mm h^{-1} precipitation objects during the peak convective forecast hours (12–24 h). The frequency of forecast and observed objects per day is summarized in Figure 12, indicating that both the control and LISMOD tend to produce more 10 mm h^{-1} precipitation objects than observed at all peak convective forecast hours. The observed daily frequency averages from 2 to 7 objects per forecast hour while the control/LISMOD daily frequency generally averages from 4 to 12 objects per forecast hour. The matched and unmatched area for precipitation objects during the peak convective hours are summed for each control and LISMOD forecast run. Improvements correspond to increases in the matched area and decreases in the unmatched area, as summarized in Figure 13. The LISMOD individual forecasts experience varying degrees of improvement and degradation from run to run relative to the control runs (CON in Figure 13a-c). The LISMOD runs tend to have the largest increases in matched area (e.g. mid-August) and more numerous decreases in unmatched areas. However, there continues to be much more unmatched area than matched area, on the order of a 2:1 ratio or more. While some improvements have been made, the forecast improvements still needed are substantial in comparison to what the model can provide in this configuration.

A summary of the mean matched/unmatched precipitation object areas per forecast run is provided in Table 5 for each of the three accumulated precipitation thresholds examined (5, 10, and 25 mm h^{-1}). The LISMOD produces on average more matched and fewer unmatched object areas compared to the control for all three thresholds between forecast hours 12–24. The lone

exception is the matched area for 25 mm h^{-1}, in which the matched area averages the same in both the control and LISMOD. Using a standard t-test, all of the improvements in unmatched area are determined to be statistically significant at the 99th percentile, while only the 4.3% improvement in 10 mm h^{-1} matched area is marginally significant at the 90th percentile. All other changes to the matched area at other thresholds are non-significant.

The improvements to the forecast precipitation are also prevalent as a function of forecast hour, at least in the 10 mm h^{-1} threshold (Figure 14). During the peak convective times, the LISMOD consistently produced a slight increase in the matched area and a slight decrease in the unmatched area as a function of forecast hour (Figure 14a). The percentage change in matched/unmatched area indicates the greatest improvement earlier in the day between forecast hours 12 and 19 (Figure 14b). The 5-mm h^{-1} threshold also shows a notable improvement in the LISMOD, mainly from a reduction in unmatched area; however, the 25-mm h^{-1} threshold does not show much of a clear distinction between the control and LISMOD as a function of forecast hour (not shown).

Figure 15 provides a summary of the overall distribution of interest function values between forecast and observed object pairs at all forecast hours between 1500–0300 UTC for all 81 forecast days (Sample sizes for each threshold are given in Table 6). Higher interest function values indicate that the forecast objects tend to be more similar in attributes to the corresponding observed objects. Among the three precipitation thresholds presented in Figure 15, the LISMOD has a larger interest value at higher percentiles in the distribution, particularly for the more intense precipitation thresholds. The LISMOD has a consistently higher interest value nearly everywhere in the distribution for the 25-mm h^{-1} threshold, and from the 50th to 90th percentiles for 10-mm h^{-1} threshold. The 5-mm h^{-1} interest values show little overall difference between

control and LISMOD. This result indicates that the LISMOD forecasts produced 1-h accumulated precipitation areas that more closely resemble the observed rainfall areas for more intense thresholds.

The reduced precipitation bias and false alarm objects combined with an increase in object hits suggest that higher-resolution land surface (particularly soil moisture) and SSTs in the LISMOD lead to some improvements in the surface heating rates, PBL evolution, and subsequent mesoscale circulations. If the changes from generally drier regional soil moisture in LISMOD were purely systematic, then one would expect to see only a decrease in the bias and false alarm objects, and not any improvements to the matched objects. Despite the slight improvements to verification results, the skill scores and false alarm rate are still low, indicating the model's inability to predict accurately diurnal convection over the southeastern U.S. under weakly-forced conditions.

5. Summary and conclusions

This paper presents results from a numerical modeling sensitivity experiment in which the interpolated land and ocean surface fields from the NCEP NAM model in a control WRF model simulation are replaced with high-resolution datasets provided by unique NASA assets in an experimental simulation: the LIS and SPoRT/MODIS SSTs. The LIS is run in an offline mode for several years at the same grid resolution as the WRF model in order to provide WRF with compatible land surface initial conditions in an equilibrium state. The MODIS SSTs provide more detailed analyses of the SSTs over the oceans and large lakes compared to the RTG product used in the control model runs.

Results indicate that the LISMOD initial conditions contain much more detail, consistent with the WRF model resolution, when compared to the control initial conditions. The large-scale

patterns of soil moisture are fairly similar, but the LISMOD initial conditions do have some systematic regional differences, probably due to the LIS better resolving the fine-scale precipitation features of the Stage IV data compared to the 12-km NDAS. The MODIS SSTs are better able to capture the spatial variability in SSTs, especially in the waters surrounding the Florida peninsula. The LIS soil moisture and MODIS SSTs are shown to have substantial impacts on the sensible heat flux, 2-m dew points, PBL height, and CAPE. On 9 June, the CAPE is reduced over areas of drier soil moisture due to the decrease in low-level moisture diffused through a deeper PBL. The forecast precipitation fields are fairly similar, especially in the overall larger-scale patterns; however, numerous small-scale differences occur due to the variations in soil moisture distribution in the initial conditions.

Traditional verification methods of 2-m temperature and dew point do not reveal substantial differences between the two forecast configurations. Only slight differences in the 2-m temperature and dew point errors are evident. The traditional grid point precipitation verification does show a small reduction in the over-prediction of rainfall areas in LISMOD; however, the skill is almost equally low in both experiments. Output from MODE's object-based verification within the MET package reveals that the LISMOD consistently generated precipitation objects that better matched observed precipitation objects, especially at higher precipitation intensities. For the 1-h accumulated precipitation thresholds examined, the LISMOD runs produce an increase in matched precipitation areas and a simultaneous decrease in unmatched areas in most instances (i.e. increase in hits and decrease in combined false alarms and forecast misses). This result suggests that the LISMOD did not just simply decrease precipitation production due to a drier soil solution. Instead, the increased resolution of the surface initial conditions most likely impacted the local surface heating rates in a positive sense, resulting in a slight improvement to

the PBL evolution and simulated mesoscale circulations. However, the overall low verification scores indicate that much uncertainty still exists in simulating the processes responsible for air-mass type convective precipitation in convection-allowing models.

Since this experiment was conducted, the NASA SPoRT Center developed an enhanced SST algorithm that improves upon the MODIS-only composites by incorporating microwave SST information from the Advanced Microwave Scanning Radiometer - Earth Observing System sensor aboard NASA's Aqua satellite (Vasquez et al. 2009). Schiferl et al. (2010) documented the improvements to the SST verification as well as some forecast improvements realized by this new algorithm around south Florida. Improvements could also be realized in the land surface initialization by replacing the coarse resolution, somewhat dated climatology fields of monthly vegetation and albedo with real composite data from the NASA MODIS instrument. Crawford et al. (2001), Kurkowski et al. (2003), and James et al. (2009) each demonstrated the potential utility of such datasets derived from AVHRR data in a real-time modeling system through improvements realized in forecast low-level temperature, moisture, and near-storm environmental parameters. Trier et al. (2010) recently documented improvements to the timing of convective initiation by modifying the default WRF-ARW formulation for surface exchange to be a function of vegetation type. A more accurate representation of ocean and land surface fields, and better representations of the physical processes would all lead to improved simulations of the surface energy budget and transport of heat and moisture into the atmosphere, thus potentially leading to better convective precipitation forecasts.

Acknowledgements.

This research was funded by Dr. Tsengdar Lee of the NASA Science Mission Directorate's Earth Science Division in support of the SPoRT program at the NASA MSFC. Computational

resources for this work were provided by the NASA Center for Computational Sciences at the NASA Goddard Space Flight Center. The lead author is indebted to the invaluable assistance provided by John Halley-Gotway and others on the MET development team at NCAR. The authors also greatly appreciate the valuable contributions by three anonymous reviewers and Dr. Joseph Santanello of the Goddard Space Flight Center.

Mention of a copyrighted, trademarked or proprietary product, service, or document does not constitute endorsement thereof by the authors, ENSCO Inc., SAIC, USRA, the SPoRT Center, the National Aeronautics and Space Administration, or the United States Government. Any such mention is solely for the purpose of fully informing the reader of the resources used to conduct the work reported herein.

REFERENCES

Avissar, R., and R. A. Pielke, 1989: A parameterization of heterogeneous land surfaces for atmospheric numerical models and its impact on regional meteorology. *Mon. Wea. Rev.,* **117,** 2113-2136.

Baker, R. D., B. H. Lynn, A. Boone, W-K. Tao, and J. Simpson, 2001: The influence of soil moisture, coastline curvature, and land-breeze circulations on sea-breeze-initiated precipitation. *J. Hydrometeor.,* **2,** 193-211.

Briegleb, B. P., P. Minnis, V. Ramanathan, and E. Harrison, 1986: Comparison of regional clear-sky albedos inferred from satellite observations and model computations. *J. Climate Appl. Meteor.,* **25,** 214-226.

Brown, B. G., R. Bullock, J. Halley Gotway, D. Ahijevych, C. Davis, E. Gilleland, and L. Holland, 2007: Application of the MODE object-based verification tool for the evaluation of model precipitation fields. Preprints, *22nd Conf. on Weather Analysis and Forecasting and 18th Conf. on Numerical Weather Prediction*, Park City, UT, Amer. Meteor. Soc., 10A.2. [Available online at http://ams.confex.com/ams/pdfpapers/124856.pdf]

Brown, B. G., J. H. Gotway, R. Bullock, E. Gilleland, T. Fowler, D. Ahijevych, and T. Jensen, 2009: The Model Evaluation Tools (MET): Community tools for forecast evaluation. Preprints, *25th Conf. on International Interactive Information and Processing Systems (IIPS) for Meteorology, Oceanography, and Hydrology*, Phoenix, AZ, Amer. Meteor. Soc., 9A.6. [Available online at http://ams.confex.com/ams/pdfpapers/151349.pdf]

Case, J. L., W. L. Crosson, S. V. Kumar, W. M. Lapenta, and C. D. Peters-Lidard, 2008: Impacts of High-Resolution Land Surface Initialization on Regional Sensible Weather Forecasts from the WRF Model. *J. Hydrometeor.,* **9,** 1249-1266.

Case, J. L., J. Manobianco, A. V. Dianic, M. M. Wheeler, D. E. Harms, and C. R. Parks, 2002: Verification of high-resolution RAMS forecasts over east-central Florida during the 1999 and 2000 summer months. *Wea. Forecasting,* **17,** 1133-1151.

Chen, F., and R. Avissar, 1994a: The impact of land-surface wetness on mesoscale heat fluxes. *J. Appl. Meteor.,* **33,** 1324–1340.

Chen, F., and R. Avissar, 1994b: Impact of land-surface moisture variability on local shallow convective cumulus and precipitation in largescale models. *J. Appl. Meteor.,* **33,** 1382–1401.

Chen, F., and J. Dudhia, 2001: Coupling an advanced land-surface/hydrology model with the Penn State/NCAR MM5 modeling system. Part I: Model description and implementation. *Mon. Wea. Rev.,* **129,** 569-585.

Cosgrove, B. A., and Coauthors, 2003a: Real-time and retrospective forcing in the North American Land Data Assimilation System (NLDAS) project. *J. Geophys. Res.,* **108(D22),** 8842, doi:10.1029/2002JD003118, 2003.

Cosgrove, B. A., and Coauthors, 2003b: Land surface model spin-up behavior in the North American Land Data Assimilation System (NLDAS). *J. Geophys. Res.,* **108(D22),** 8845, doi:10.1029/2002JD003316.

Crawford, T. M., D. J. Stensrud, F. Mora, J. W. Merchant, and P. J. Wetzel, 2001: Value of incorporating satellite-derived land cover data in MM5/PLACE for simulating surface temperatures. *J. Hydrometeor.,* **2,** 453-468.

Davis, C., B. Brown, and R. Bullock, 2006: Object-based verification of precipitation forecasts. Part I: Methodology and application to mesoscale rain areas. *Mon Wea. Rev.*, **134,** 1772-1784.

Davis, C. A., B. G. Brown, R. Bullock, and J. Halley-Gotway, 2009: The Method for Object-based Diagnostic Evaluation (MODE) applied to numerical forecasts from the 2005 NSSL/SPC Spring Program. *Wea. Forecasting,* **24,** 1252-1267.

Derber, J. C., D. F. Parrish, and S. J. Lord, 1991: The new global operational analysis system at the National Meteorological Center. *Wea. Forecasting,* **6,** 538-547.

Dudhia, J., 1989: Numerical study of convection observed during the winter monsoon experiment using a mesoscale two-dimensional model. *J. Atmos. Sci.,* **46,** 3077-3107.

Ek, M. B., K. E. Mitchell, Y. Lin, E. Rogers, P. Grunmann, V. Koren, G. Gayno, and J. D. Tarpley, 2003: Implementation of Noah land surface model advances in the National Centers for Environmental Prediction operational mesoscale Eta model. *J. Geophys. Res.,* **108 (D22),** 8851, doi:10.1029/2002JD003296.

Eltahir, E. A., 1998: A soil moisture-rainfall feedback mechanism: 1. Theory and observations. *Water Resour. Res.,* **34,** 765-776.

Findell, K. L., and E. A. Eltahir, 2003: Atmospheric controls on soil moisture-boundary layer interactions. Part II: Feedbacks within the Continental United States. *J. Hydrometeor.,* **4,** 570-583.

Godfrey, C. M., and D. J. Stensrud, 2008: Soil temperature and moisture errors in the operational Eta model analyses. *J. Hydrometeor.,* **9,** 367-387.

Goodman, S. J., W. M. Lapenta, G. J. Jedlovec, J. C. Dodge, and J. T. Bradshaw, 2004: The NASA Short-term Prediction Research and Transition (SPoRT) Center: A collaborative model for accelerating research into operations. 20th Conf. on Interactive Information Processing Systems (IIPS) for Meteorology, Oceanography, and Hydrology, Seattle, WA, Amer. Meteor. Soc., P1.34. [Available online at http://ams.confex.com/ams/pdfpapers/70210.pdf]

Gutman, G. and A. Ignatov, 1998: Derivation of green vegetation fraction from NOAA/AVHRR for use in numerical weather prediction models. *Int. J. Remote Sensing,* **19,** 1533-1543.

Haines, S. L., G. J. Jedlovec, and S. M. Lazarus, 2007: A MODIS sea surface temperature composite for regional applications. *IEEE Trans. Geosci. Remote Sens.,* **45,** 2919-2927.

Hong, S.-Y., and J-O J. Lim, 2006: The WRF single-moment 6-class microphysics scheme (WSM6). *J. Korean Meteor. Soc.,* **42,** 129-151.

James, K. A., D. J. Stensrud, and N. Yussouf, 2009: Value of real-time vegetation fraction to forecasts of severe convection in high-resolution models. *Wea. Forecasting,* **24,** 187-210.

Janjić, Z. I., 1990: The step-mountain coordinate: Physical package. *Mon. Wea. Rev.,* **118,** 1429–1443.

Janjić, Z. I., 1996: The surface layer in the NCEP Eta Model. Preprints, *Eleventh Conference on Numerical Weather Prediction,* Norfolk, VA, Amer. Meteor. Soc., 354–355.

Janjić, Z. I., 2002: Nonsingular Implementation of the Mellor–Yamada Level 2.5 Scheme in the NCEP Meso model, NCEP Office Note, No. 437, 61 pp.

Kain, J. S., S. R. Dembek, S. J. Weiss, J. L. Case, J. J. Levitt, and R. A. Sobash, 2010: Extracting unique information from high-resolution forecast models: Monitoring selected fields and phenomena every time step. *Wea. Forecasting,* **25,** 1536-1542.

Koster, R. D., and M. J. Suarez, 2003: Impact of land surface initialization on seasonal precipitation and temperature prediction. *J. Hydrometeor.,* **4,** 408–423.

Koster, R. D., M. J. Suarez, M. Heiser, 2000: Variance and predictability of precipitation at seasonal-to-interannual timescales. *J. Hydrometeor.,* **1,** 26-46.

Koster, R. D., and Coauthors, 2004: Realistic initialization of land surface states: Impacts on subseasonal forecast skill. *J. Hydrometeor.,* **5,** 1049-1063.

Koster, R. D., and Coauthors, 2006: GLACE: The Global Land-atmosphere Coupling Experiment. Part I: Overview. *J. Hydrometeor.,* **7,** 590-610.

Kumar, S. V., and Coauthors, 2006: Land Information System – An Interoperable Framework for High Resolution Land Surface Modeling. *Environmental Modeling & Software,* **21 (10),** 1402-1415, doi:10.1016/j.envsoft.2005.07.004.

Kumar, S. V., C. D. Peters-Lidard, J. L. Eastman, and W.-K. Tao, 2007: An integrated high-resolution hydrometeorological modeling testbed using LIS and WRF. *Environmental Modeling & Software,* **23 (2),** 169-181, doi: 10.1016/j.envsoft.2007.05.012.

Kumar, S. V., R. H. Reichle, R. D. Koster, W. T. Crow, C. D. Peters-Lidard, 2009: Role of subsurface physics in the assimilation of surface soil moisture observations. *J. Hydrometeor.,* **10,** 1534-1547.

Kurkowski, N. P., D. J. Stensrud, and M. E. Baldwin, 2003: Assessment of implementing satellite-derived land cover data in the Eta model. *Wea. Forecasting,* **18,** 404-416.

LaCasse, K. M., M. E. Splitt, S. M. Lazarus, and W. M. Lapenta, 2008: The impact of high-resolution sea surface temperatures on the simulated nocturnal Florida marine boundary layer. *Mon. Wea. Rev.,* **136,** 1349-1372.

Lin, Y., and K. E. Mitchell, 2005: The NCEP Stage II/IV hourly precipitation analyses: Development and applications. Preprints, *19th Conf. on Hydrology,* San Diego, CA, Amer. Meteor. Soc., 1.2. [Available online at http://ams.confex.com/ams/pdfpapers/83847.pdf]

Lin, Y., K. E. Mitchell, E. Rogers, and G. J. DiMego, 2005: Using hourly and daily precipitation analyses to improve model water budget. Preprints, *Ninth Symp. on Integrated Observing and Assimilation Systems for the Atmosphere, Oceans, and Land Surface*, San Diego, CA, Amer. Meteor. Soc., 3.3. [Available online at http://ams.confex.com/ams/pdfpapers/84484.pdf]

Marshall, C. H., K. C. Crawford, K. E. Mitchell, and D. J. Stensrud, 2003: The impact of the land surface physics in the operational NCEP Eta model on simulating the diurnal cycle: Evaluation and testing using Oklahoma Mesonet data. *Wea. Forecasting,* **18,** 748-768.

Miller, D. A. and R. A. White, 1998: A Conterminous United States multi-layer soil characteristics data set for regional climate and hydrology modeling. *Earth Interactions*, 2. [Available on-line at http://EarthInteractions.org].

Mlawer, E. J., S. J. Taubman, P. D. Brown, M. J. Iacono, and S. A. Clough, 1997: Radiative transfer for inhomogeneous atmosphere: RRTM, a validated correlated-k model for the long-wave. *J. Geophys. Res.,* **102 (D14),** 16663-16682.

Ookouchi, Y., M. Segal, R. C. Kessler, and R. A. Pielke, 1984: Evaluation of soil moisture effects on the generation and modification of mesoscale circulations. *Mon. Wea. Rev.,* **112,** 2281-2292.

Reichle, R. H., R. D. Koster, P. Lui, S. P. P. Mahanama, E. G. Njoku, and M. Owe, 2007: Comparison and assimilation of global soil moisture retrievals from the Advanced Microwave Scanning Radiometer for the Earth Observing System (AMSR-E) and the Scanning Multichannel Microwave Radiometer (SMMR). *J. Geophys. Res.,* **112 (D09108),** doi:10.1029/2006JD008033.

Robinson, D. A. and G. Kukla, 1985: Maximum surface albedo of seasonally snow covered lands in the Northern Hemisphere. *J. Climate Appl. Meteor.,* **24,** 402-411.

Robock, A., and Coauthors, 2003: Evaluation of the North American Land Data Assimilation System over the southern Great Plains during the warm season. *J. Geophys. Res.,* **108 (D22),** 8846, doi:10.1029/2002JD003245.

Rodell, M., P. R. Houser, A. A. Berg, and J. S. Famiglietti, 2005: Evaluation of 10 methods for initializing a land surface model. *J. Hydrometeor.,* **6,** 146-155.

Santanello, J. A. Jr., C. D. Peters-Lidard, S. V. Kumar, C. Alonge, and W-K. Tao, 2009: A modeling and observational framework for diagnosing local land-atmosphere coupling on diurnal time scales. *J. Hydrometeor.,* **10,** 577-599.

Schaefer, G. L., M. H. Cosh, and T. J. Jackson, 2007: The USDA Natural Resources Conservation Service Soil Climate Analysis Network (SCAN). *J. Atmos. Oceanic Technol.,* **24,** 2073-2077.

Schiferl, L., K. K. Fuell, J. L. Case, and G. J. Jedlovec, 2010: Evaluation of enhanced high resolution MODIS/AMSR-E SSTs and the impact on regional weather forecasts. Preprints, *14th Symp. on Integrated Observing and Assimilation Systems for the Atmosphere, Oceans,*

and Land Surface, Atlanta, GA, Amer. Meteor. Soc., P535. [Available online at http://ams.confex.com/ams/pdfpapers/163774.pdf]

Skamarock, W. C., J. B. Klemp, J. Dudhia, D. O. Gill, D. M. Barker, M. G. Duda, X-Y. Huang, W. Wang and J. G. Powers, 2008: A Description of the Advanced Research WRF Version 3, NCAR Technical Note, NCAR/TN–475+STR, 123 pp. [Available on-line at: http://www.mmm.ucar.edu/wrf/users/docs/arw_v3.pdf]

Skamarock, W. C., and M. L. Weisman, 2009: The impact of positive-definite moisture transport on NWP precipitation forecasts. *Mon. Wea. Rev.,* **137,** 488-494..

Smagorinsky J., S. Manabe, and J. L. Holloway Jr., 1965: Numerical results from a nine-level general circulation model of the atmosphere. *Mon. Wea. Rev*, **93**, 727–768.

Trier, S. B., F. Chen, and K. W. Manning, 2004: A study of convection initiation in a mesoscale model using high-resolution land surface initial conditions. *Mon. Wea. Rev.,* **132,** 2954-2976.

Trier, S. B., F. Chen, K. W. Manning, M. A. LeMone, and C. A. Davis, 2008: Sensitivity of the PBL and precipitation in 12-day simulations of warm-season convection using different land surface models and soil wetness conditions. *Mon. Wea. Rev.,* **136,** 2321-2343.

Trier, S. B., M. A. LeMone, F. Chen, and K. W. Manning, 2010:Effects of surface heat and moisture exchange on ARW-WRF warm-season precipitation forecasts over the Central United States. *Wea. Forecasting, In Press.* [Available through early online release at http://journals.ametsoc.org/doi/pdf/10.1175/2010WAF2222426.1]

Vazquez, J, T. M. Chin, E. Armstrong, and G. Jedlovec, 2009: A comparison of 1km ultra high resolution composite SST maps. Preprints, *Proceedings from the GHRSST User Symposium,* May 28-29, 2009, Santa Rosa, CA.

Zeng, X., and A. Beljaars, 2005: A prognostic scheme of sea surface skin temperature for modeling and data assimilation. *Geophys. Res. Lett.,* **32,** 14605, doi:10.1029/2005GL023030.

Figure Captions

Figure 1. Change in volumetric soil moisture (%) in the Noah 40−100 cm layer for the 0300 UTC WRF initializations from 18–26 August 2008, valid for the (a) control run, and (b) LISMOD run; (c) total Stage IV rainfall (mm), accumulated from 0000 UTC 18 Aug to 0000 UTC 26 Aug, and (d) time-depth cross section of LIS/Noah volumetric soil moisture at 31°N, 84°W (denoted by the 'X' in panel b over southwestern Georgia).

Figure 2. Comparison between WRF-initialized 0–10 cm volumetric soil moisture for the (a) control (NAM model), (b) LIS spin-up, and (c) difference field (LIS – control) valid at 0300 UTC 9 June 2008. The region depicted is the horizontal extent of the 4-km model domain.

Figure 3. Location of Soil Climate Analysis Network (SCAN) observations used to validate the NCEP/NAM (control) and LIS volumetric soil moisture (%) and soil temperature at the model initialization times.

Figure 4. Time series of spatial-averaged observed, control, and LISMOD volumetric soil moisture and daily anomalies (in %) at SCAN observations locations for each model initialization time for (a) 5-cm level soil moisture, (b) 5-cm level soil moisture anomaly, (c) weighted root zone soil moisture, and (d) weighted root zone soil moisture anomaly. Gaps in the time series indicate days with missing MODIS SSTs, and thus, no model forecasts.

Figure 5. Time series of spatial-averaged soil temperatures (K) at SCAN observation locations for each model initialization time at the (a) 5-cm level, and (b) weighted root zone. Gaps in the time series indicate days with missing MODIS SSTs, and thus, no model forecasts.

Figure 6. Comparison between WRF static SSTs for the (a) control (NAM model / RTG product), (b) LISMOD (SPoRT MODIS data), and (c) difference field (LISMOD – control), valid for the model run initialized at 0300 UTC 9 June 2008.

Figure 7. Difference plots (LISMOD – control) of the 13-h forecasts valid at 1600 UTC 9 June 2008 for the following fields: (a) sensible heat flux (W m^{-2}), (b) 2-m dew point temperature (°C), (c) planetary boundary layer (PBL) height in meters, and (d) convective available potential energy (CAPE, J kg^{-1}).

Figure 8. Comparison of accumulated precipitation (mm) for the 1-h period ending 2100 UTC 9 June 2008 for the (a) control run, (b) LISMOD run, (c) difference between LISMOD and control, and (d) Stage IV precipitation. Traditional grid point verification at a 10-mm threshold yields a Heidke Skill Score of 0.034 for the control run and 0.046 for the LISMOD run over this time interval.

Figure 9. Comparison of 2-m temperature and dew point temperature model errors (°C) for 81 control and LISMOD forecasts from June–August 2008 at approximately 500 surface observation locations. Plots shown are (a) mean error (bias), and (b) Error standard deviation (StDev).

Figure 10. Traditional verification metrics of accumulated precipitation for all 81 forecasts in the study period (June to August 2008). Plots shown are (a) bias of the 1-h accumulated precipitation during the peak convective hours of 1500 to 0300 UTC (forecast hours 12–24), (b) Heidke Skill Score (HSS) of the 1-h accumulated precipitation during forecast hours 12–24, (c) Threat Score (TS) of the 1-h accumulated precipitation during forecast hours 12–24, and (d) TS of the 24-h accumulated precipitation for forecast hours 3–27, according to the legends provided.

Figure 11. Comparison of 18-h forecast and Stage IV (observed) ≥10-mm accumulated precipitation objects for the 1-h period ending 2100 UTC 9 June 2008 for the (a) control run, and (b) LISMOD run. Solid blue shading indicates a false alarm in the forecast field or a forecast miss in the observed field. All other solid colors represent matched forecast or observed objects. Outlined blue areas denote the corresponding observed (forecast) objects in the field of forecast (observed) objects.

Figure 12. Frequency of forecast (control and LISMOD) and observed 10 mm h^{-1} MODE precipitation objects, representing the average number of objects per forecast hour per day over all forecast days in the period of record.

Figure 13. Comparison of Control (CON) and LIS+MODIS (LISMOD) 10 mm h^{-1} accumulated precipitation objects for (a) matched area, (b) unmatched area, and (c) difference in matched and unmatched area, summed during the peak convective hours (1500 UTC to 0300 UTC) for each individual forecast from June to August 2008.

Figure 14. Comparison between the total matched and unmatched object areas from all 81 forecast cycles for 1-h accumulated precipitation ≥ 10 mm during the forecast hours centered

on the diurnal peak convective activity (12–24 hours, valid 1500 UTC to 0300 UTC). (a) Total matched and unmatched object areas for the control and LISMOD according to the legend provided, and (b) LISMOD percentage change from the control matched/unmatched object area.

Figure 15. Distribution of the total interest function for all 81 control and LISMOD forecast/observed 1-h accumulated precipitation object pairs during the peak convective hours of 1500 to 0300 UTC. The plot depicts the control and LISMOD values within their respective interest function distributions at the 10th, 25th, 50th, 75th, and 90th percentiles for 5-mm, 10-mm, and 25-mm accumulated precipitation thresholds, according to the scale provided. The interest function sample sizes are provided in Table 6.

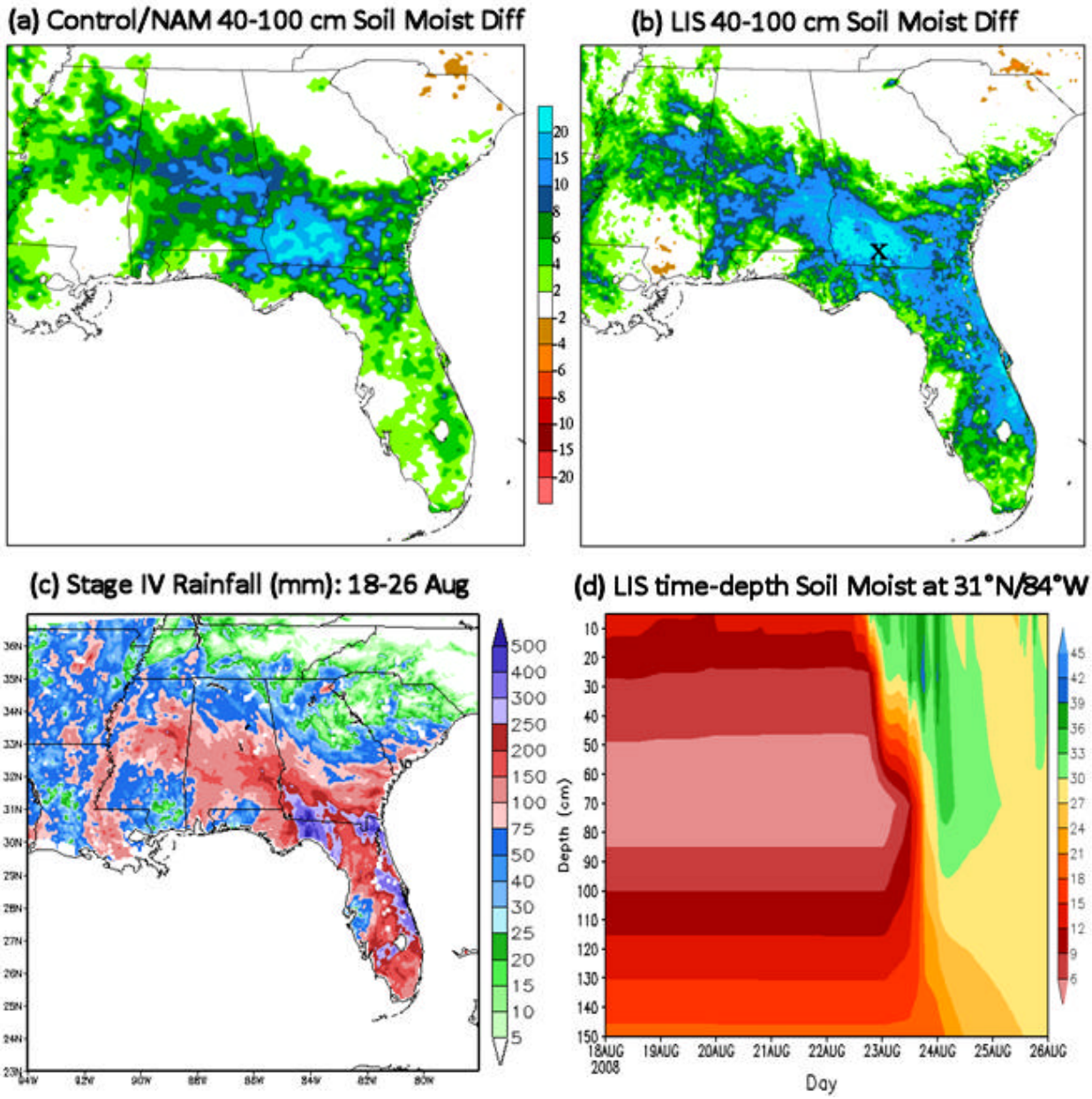

Figure 1. Change in volumetric soil moisture (%) in the Noah 40−100 cm layer for the 0300 UTC WRF initializations from 18–26 August 2008, valid for the (a) control run, and (b) LISMOD run; (c) total Stage IV rainfall (mm), accumulated from 0000 UTC 18 Aug to 0000 UTC 26 Aug, and (d) time-depth cross section of LIS/Noah volumetric soil moisture at 31°N, 84°W (denoted by the 'X' in panel b over southwestern Georgia).

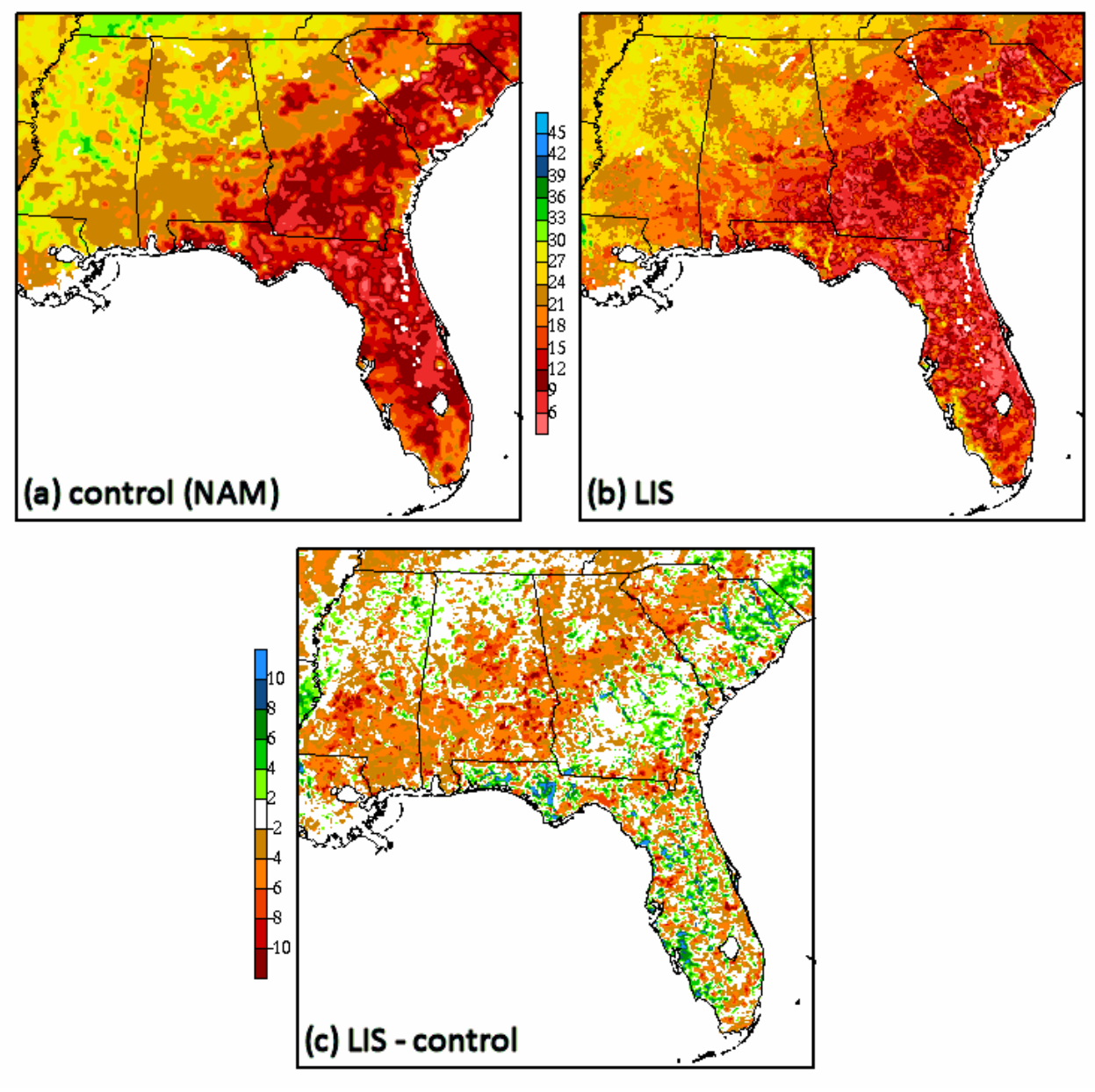

Figure 2. Comparison between WRF-initialized 0–10 cm volumetric soil moisture for the (a) control (NAM model), (b) LIS spin-up, and (c) difference field (LIS – control) valid at 0300 UTC 9 June 2008. The region depicted is the horizontal extent of the 4-km model domain.

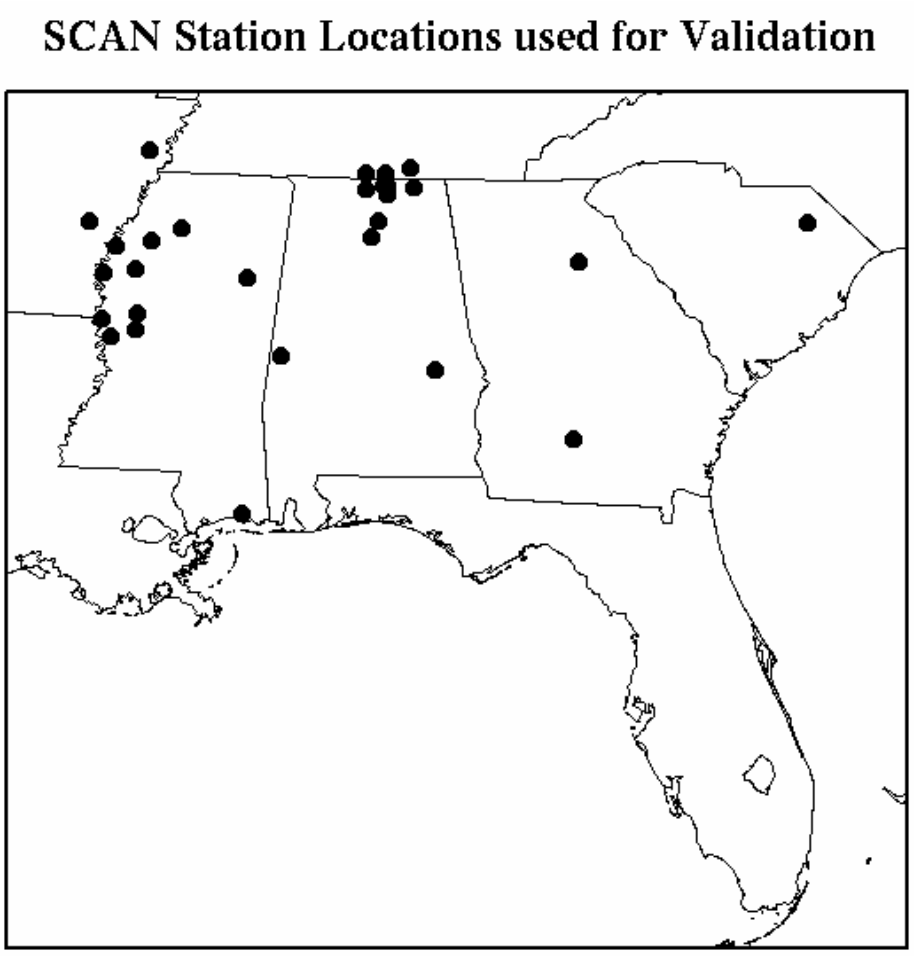

Figure 3. Location of Soil Climate Analysis Network (SCAN) observations used to validate the NCEP/NAM (control) and LIS volumetric soil moisture (%) and soil temperature at the model initialization times.

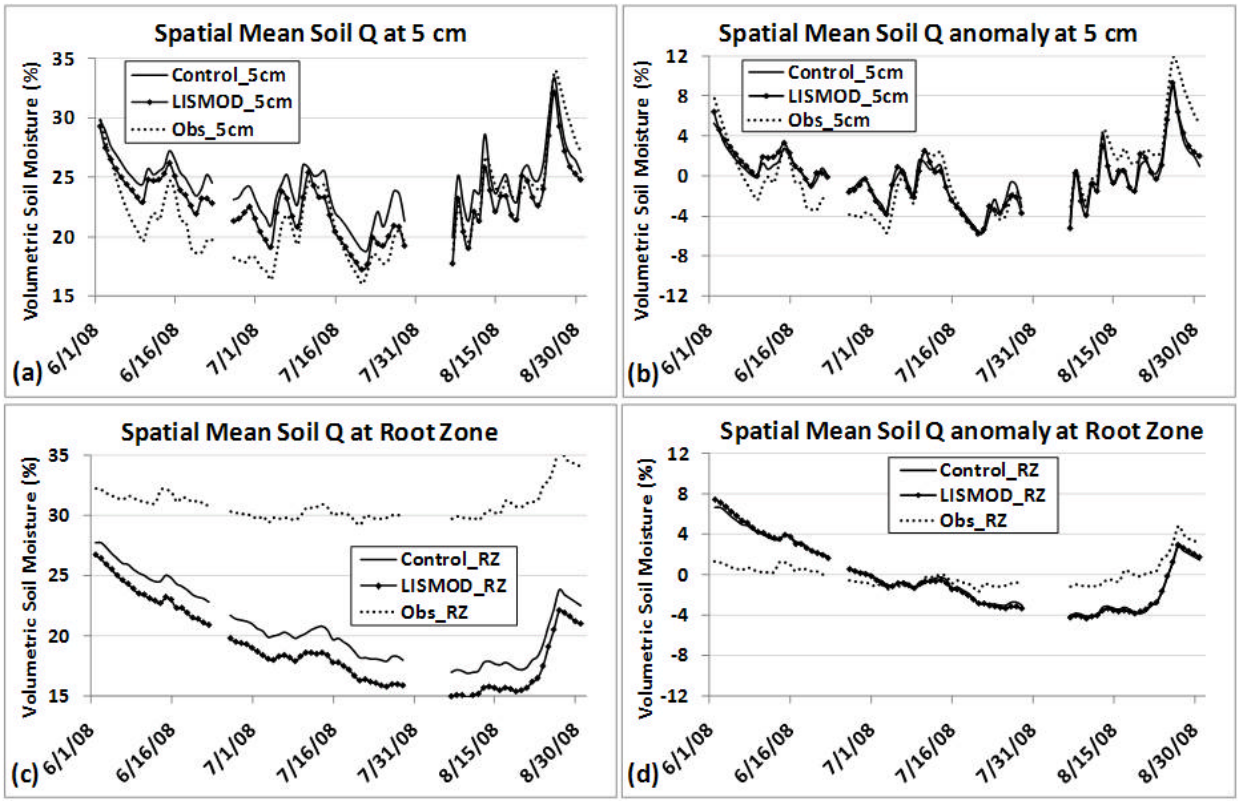

Figure 4. Time series of spatial-averaged observed, control, and LISMOD volumetric soil moisture and daily anomalies (in %) at SCAN observations locations for each model initialization time for (a) 5-cm level soil moisture, (b) 5-cm level soil moisture anomaly, (c) weighted root zone soil moisture, and (d) weighted root zone soil moisture anomaly. Gaps in the time series indicate days with missing MODIS SSTs, and thus, no model forecasts.

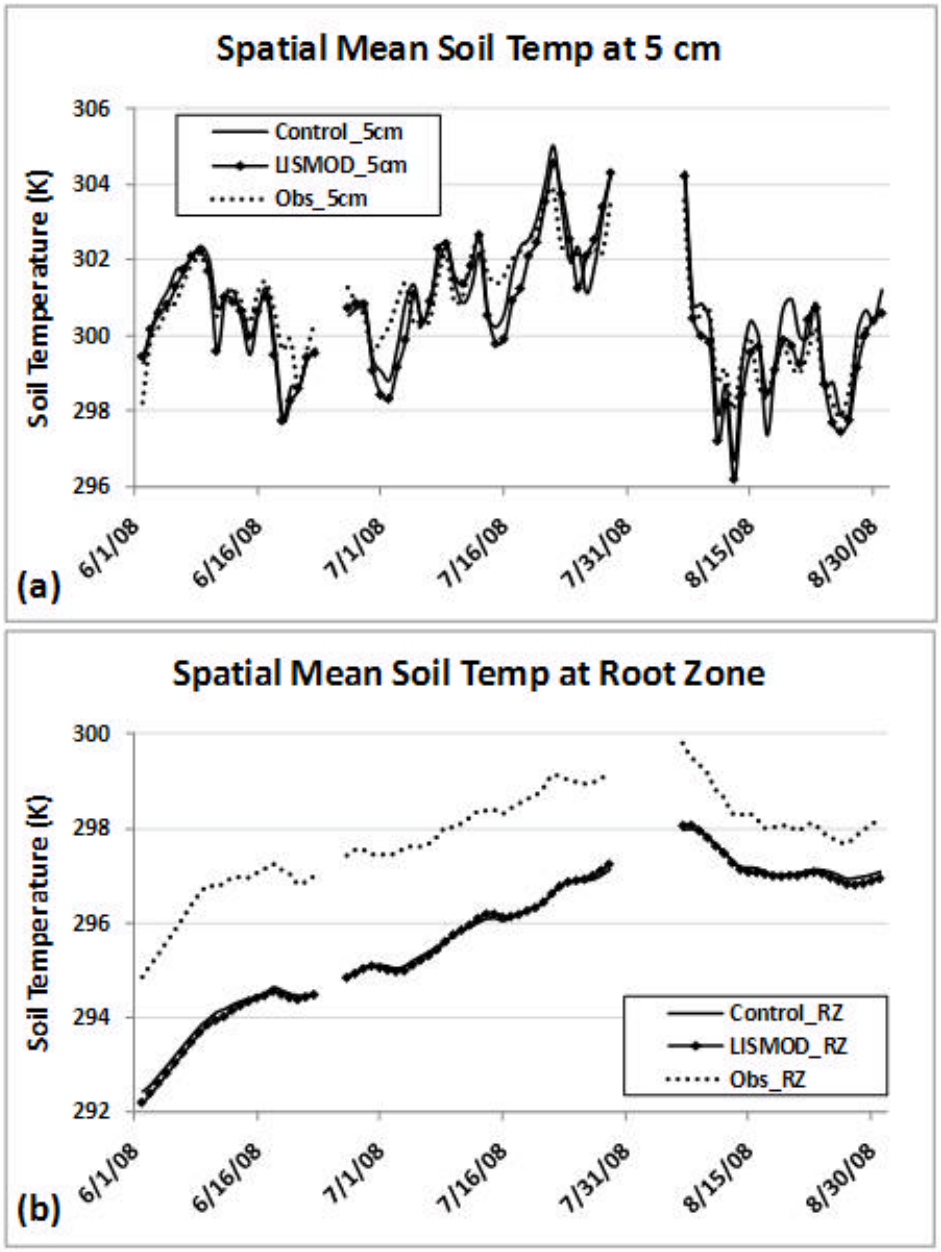

Figure 5. Time series of spatial-averaged soil temperatures (K) at SCAN observation locations for each model initialization time at the (a) 5-cm level, and (b) weighted root zone. Gaps in the time series indicate days with missing MODIS SSTs, and thus, no model forecasts.

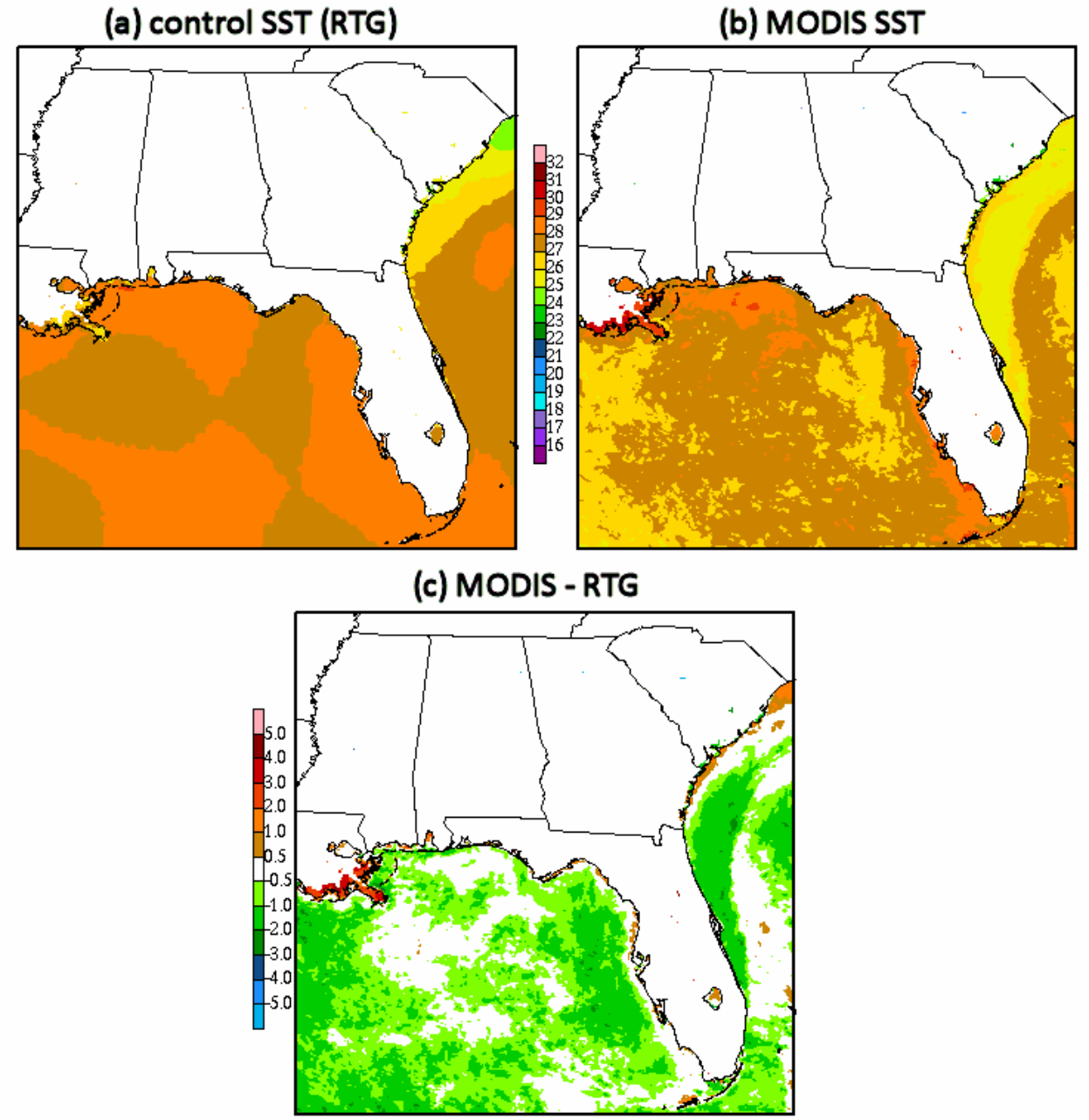

Figure 6. Comparison between WRF static SSTs for the (a) control (NAM model / RTG product), (b) LISMOD (SPoRT MODIS data), and (c) difference field (LISMOD – control), valid for the model run initialized at 0300 UTC 9 June 2008.

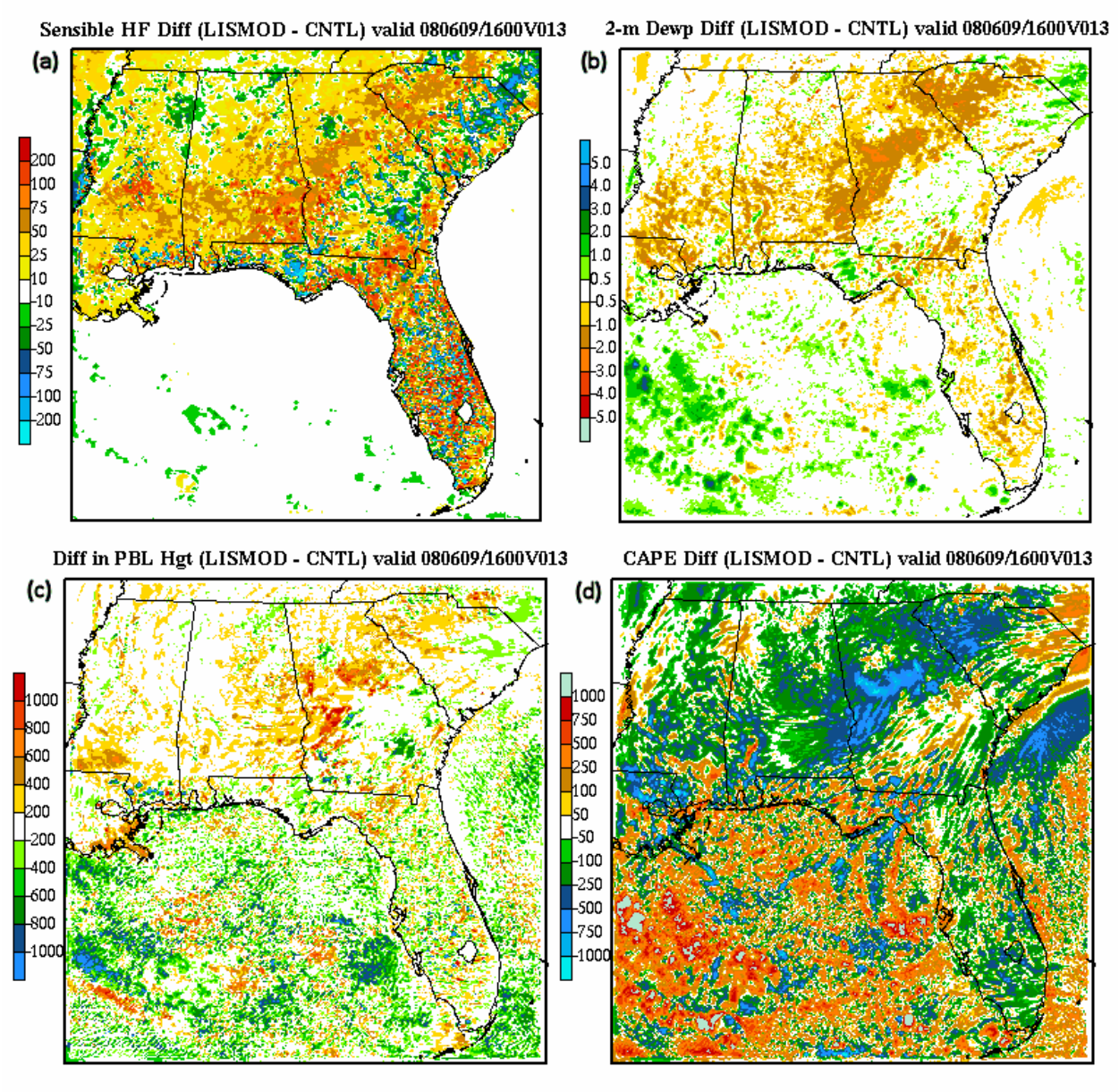

Figure 7. Difference plots (LISMOD – control) of the 13-h forecasts valid at 1600 UTC 9 June 2008 for the following fields: (a) sensible heat flux (W m^{-2}), (b) 2-m dew point temperature (°C), (c) planetary boundary layer (PBL) height in meters, and (d) convective available potential energy (CAPE, J kg^{-1}).

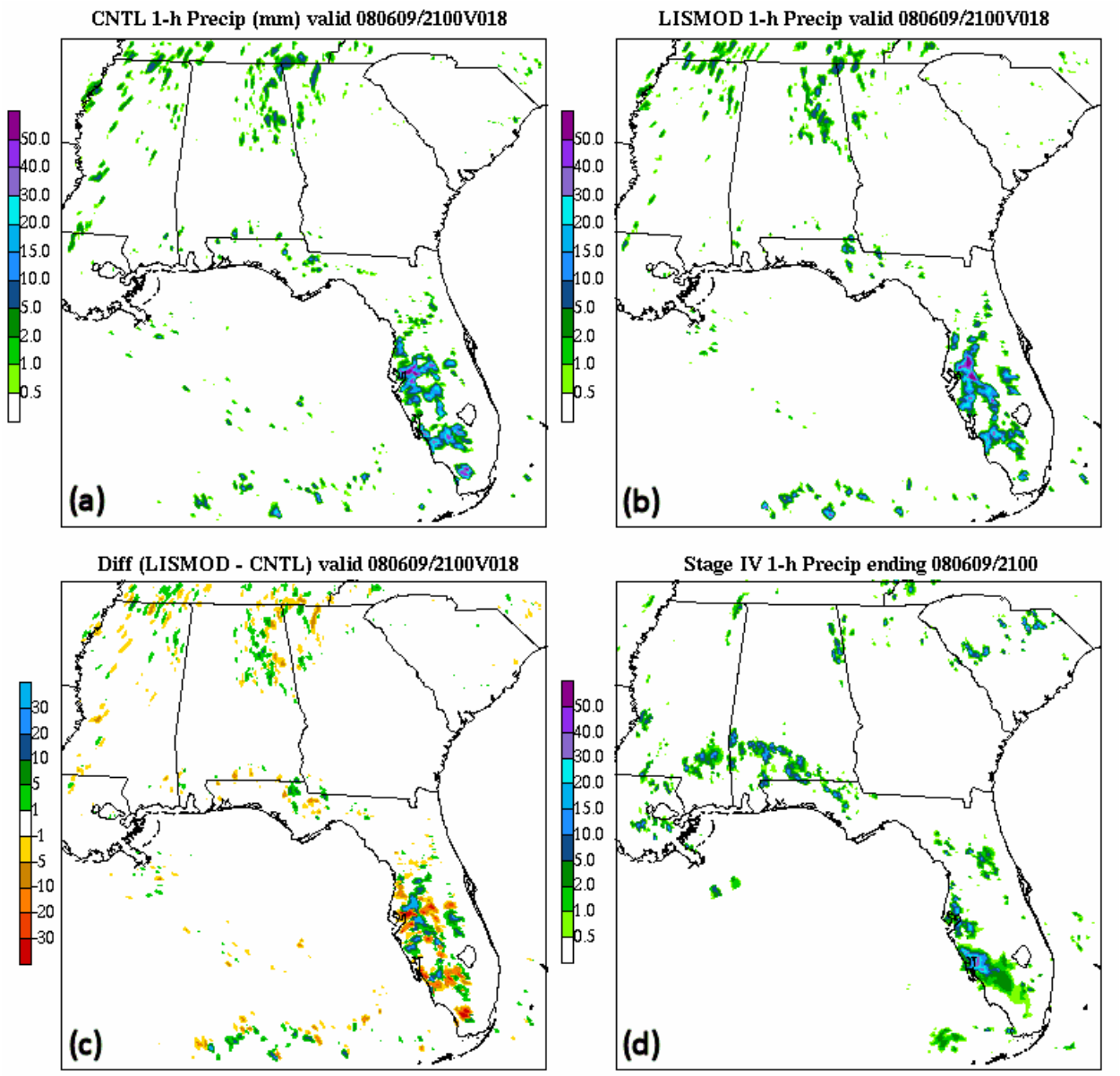

Figure 8. Comparison of accumulated precipitation (mm) for the 1-h period ending 2100 UTC 9 June 2008 for the (a) control run, (b) LISMOD run, (c) difference between LISMOD and control, and (d) Stage IV precipitation. Traditional grid point verification at a 10-mm threshold yields a Heidke Skill Score of 0.034 for the control run and 0.046 for the LISMOD run over this time interval.

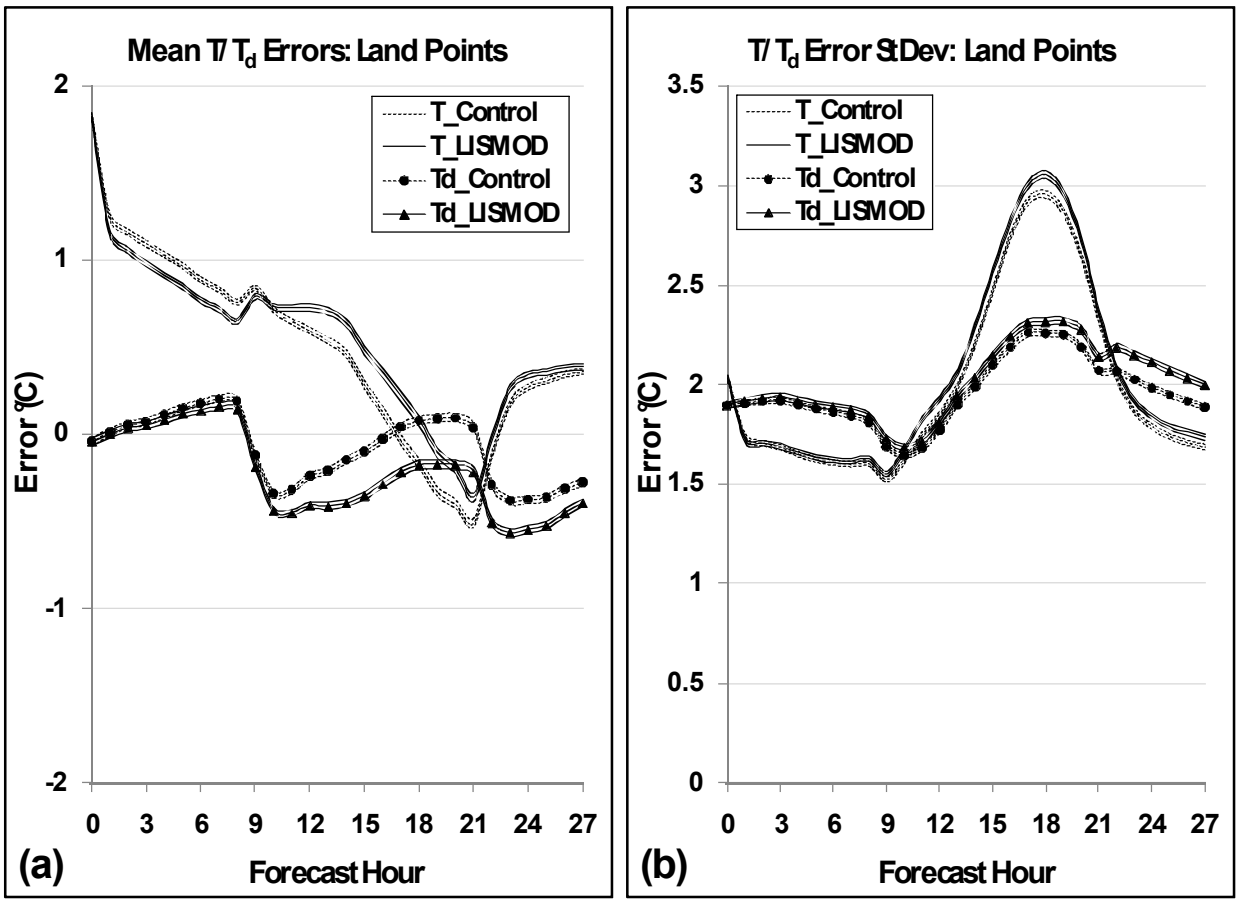

Figure 9. Comparison of 2-m temperature and dew point temperature model errors (°C) for 81 control and LISMOD forecasts from June–August 2008 at approximately 500 surface observation locations. Plots shown are (a) mean error (bias), and (b) Error standard deviation (StDev). The lower and upper confidence intervals are plotted for each series such that non-overlapping plots at a given forecast hour indicate statistical significance between the Control and LISMOD at the 95th percentile.

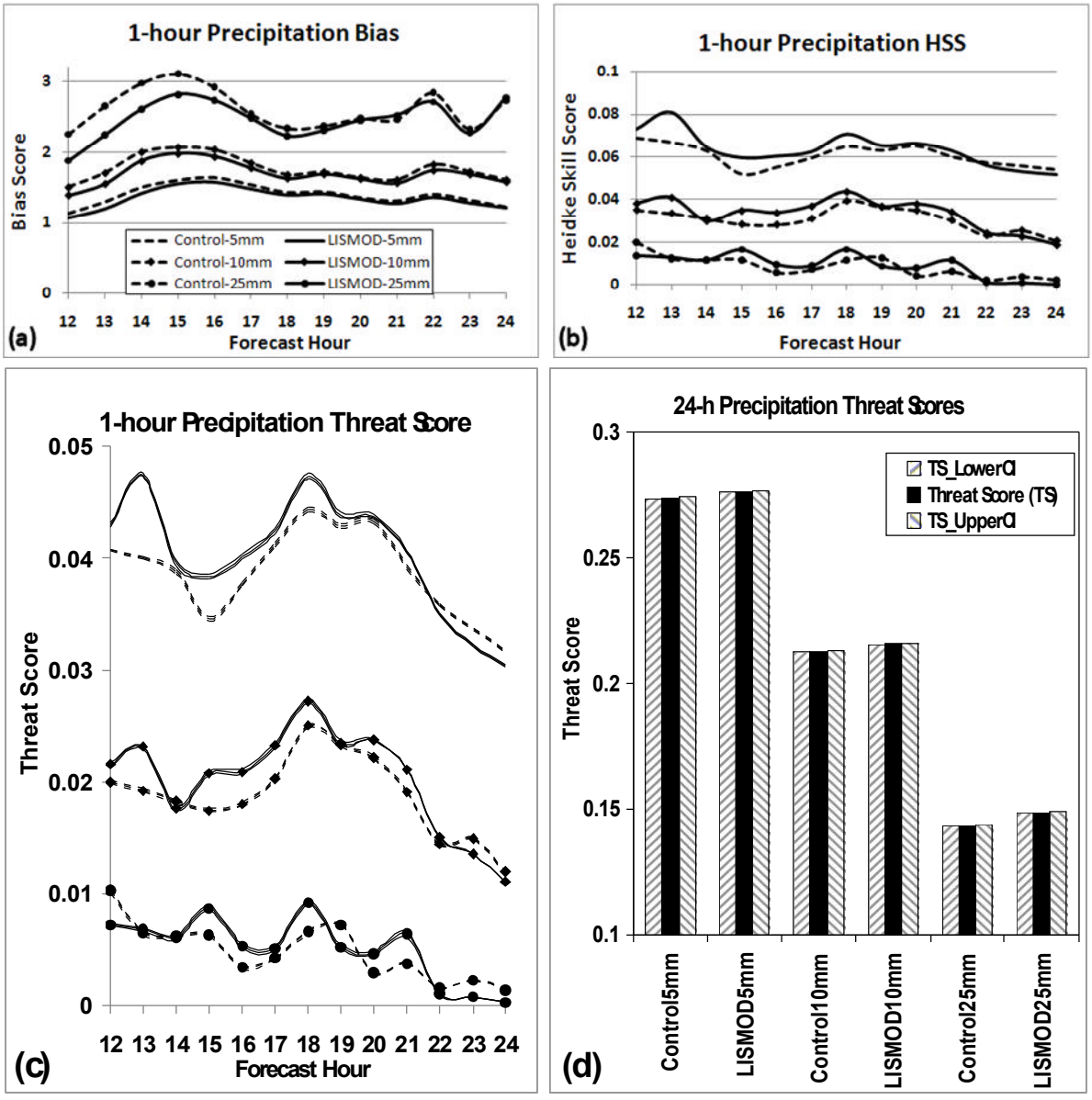

Figure 10. Traditional verification metrics of accumulated precipitation for all 81 forecasts in the study period (June to August 2008). Plots shown are (a) bias of the 1-h accumulated precipitation during the peak convective hours of 1500 to 0300 UTC (forecast hours 12–24), (b) Heidke Skill Score (HSS) of the 1-h accumulated precipitation during forecast hours 12–24, (c) Threat Score (TS) of the 1-h accumulated precipitation during forecast hours 12–24, and (d) TS of the 24-h accumulated precipitation for forecast hours 3–27, according to the legends provided. Lower and upper 95th percentile confidence levels are plotted with the threat scores in (c) and (d) such that non-overlapping plots indicate statistically significant differences.

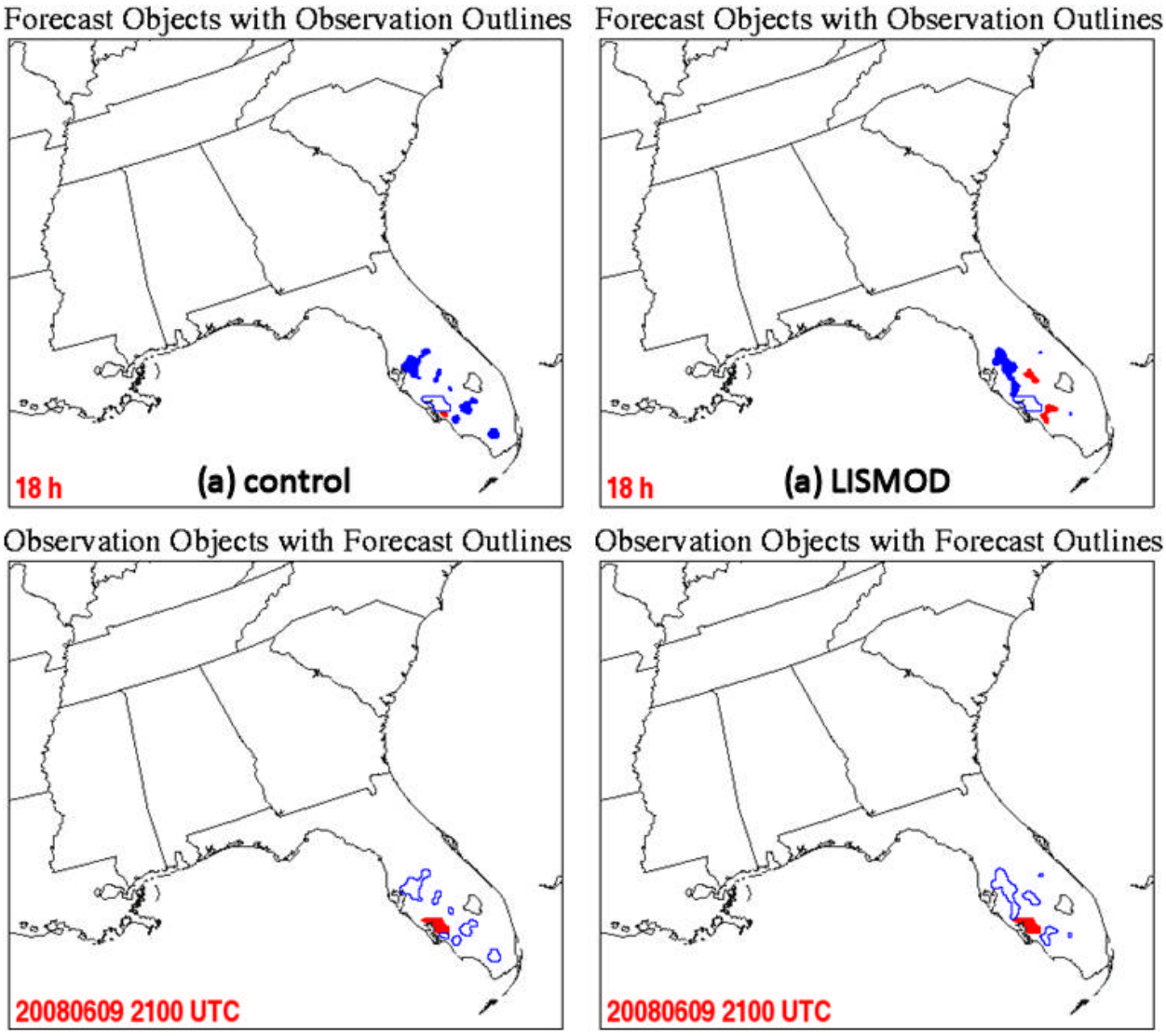

Figure 11. Comparison of 18-h forecast and Stage IV (observed) ≥10-mm accumulated precipitation objects for the 1-h period ending 2100 UTC 9 June 2008 for the (a) control run, and (b) LISMOD run. Solid blue shading indicates a false alarm in the forecast field or a forecast miss in the observed field. All other solid colors represent matched forecast or observed objects. Outlined blue areas denote the corresponding observed (forecast) objects in the field of forecast (observed) objects.

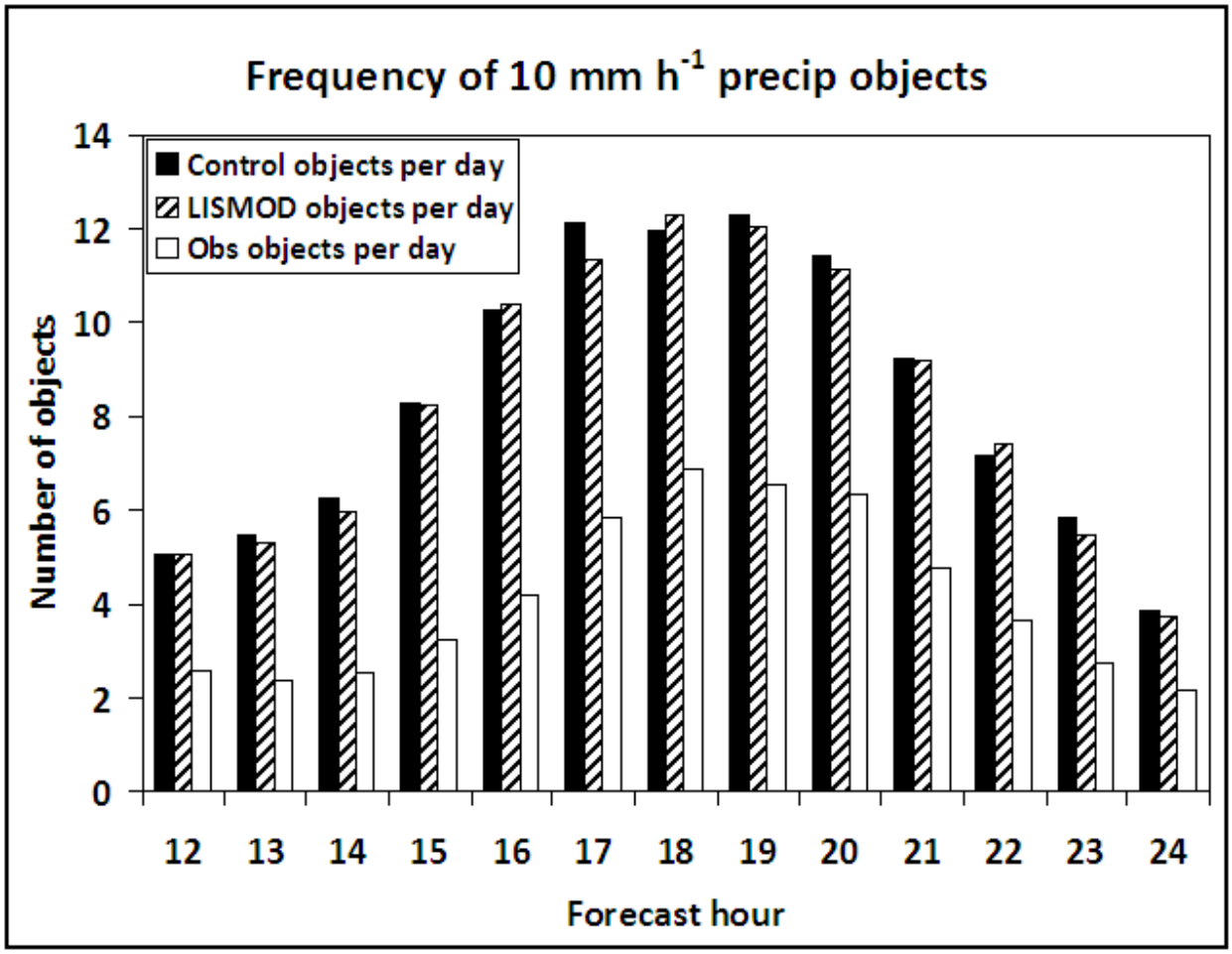

Figure 12. Frequency of forecast (control and LISMOD) and observed 10 mm h^{-1} MODE precipitation objects, representing the average number of objects per forecast hour per day over all forecast days in the period of record.

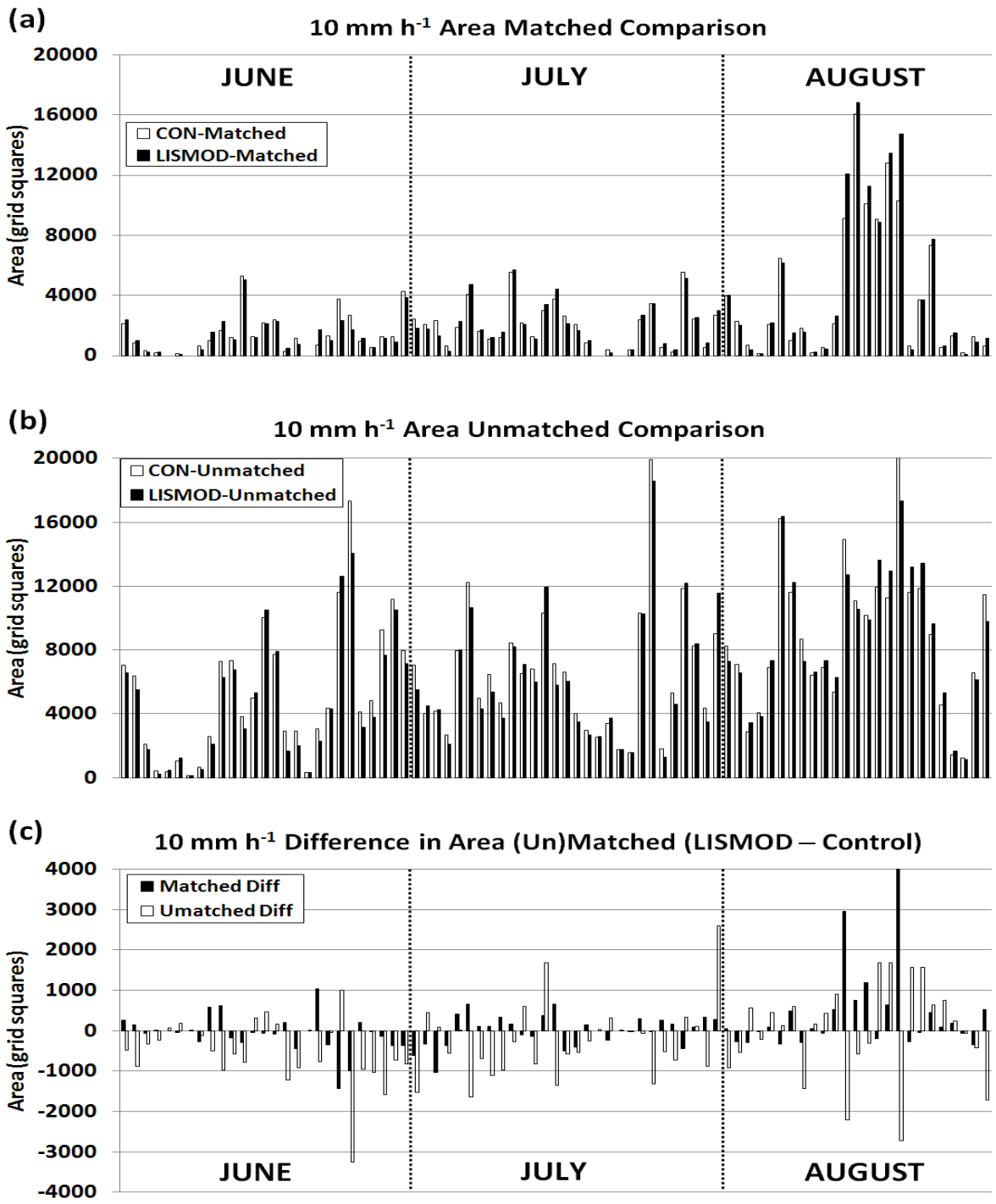

Figure 13. Comparison of Control (CON) and LIS+MODIS (LISMOD) 10 mm h^{-1} accumulated precipitation objects for (a) matched area, (b) unmatched area, and (c) difference in matched and unmatched area, summed during the peak convective hours (1500 UTC to 0300 UTC) for each individual forecast from June to August 2008.

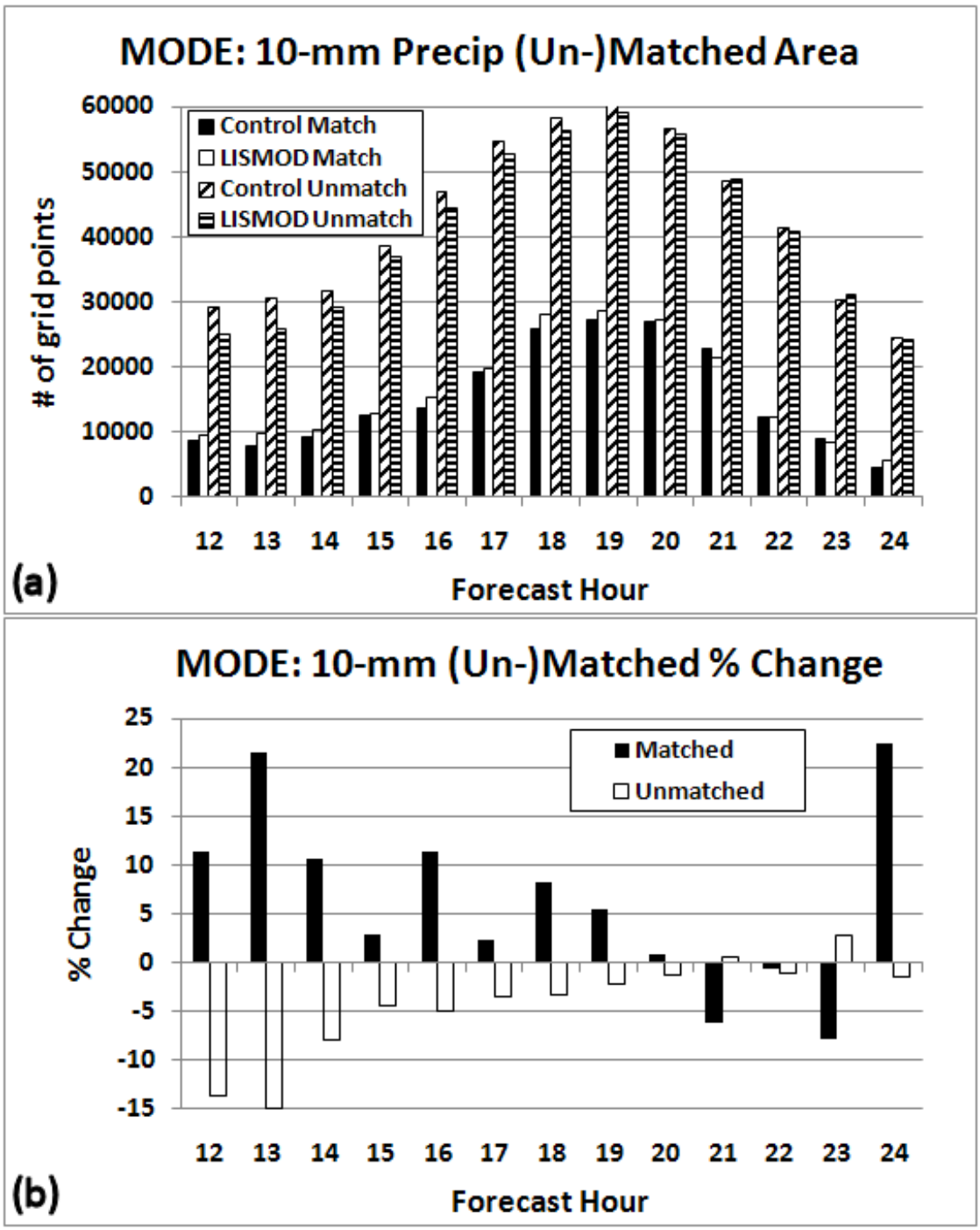

Figure 14. Comparison between the total matched and unmatched object areas from all 81 forecast cycles for 1-h accumulated precipitation ≥ 10 mm during the forecast hours centered on the diurnal peak convective activity (12–24 hours, valid 1500 UTC to 0300 UTC). (a) Total matched and unmatched object areas for the control and LISMOD according to the legend provided, and (b) LISMOD percentage change from the control matched/unmatched object area.

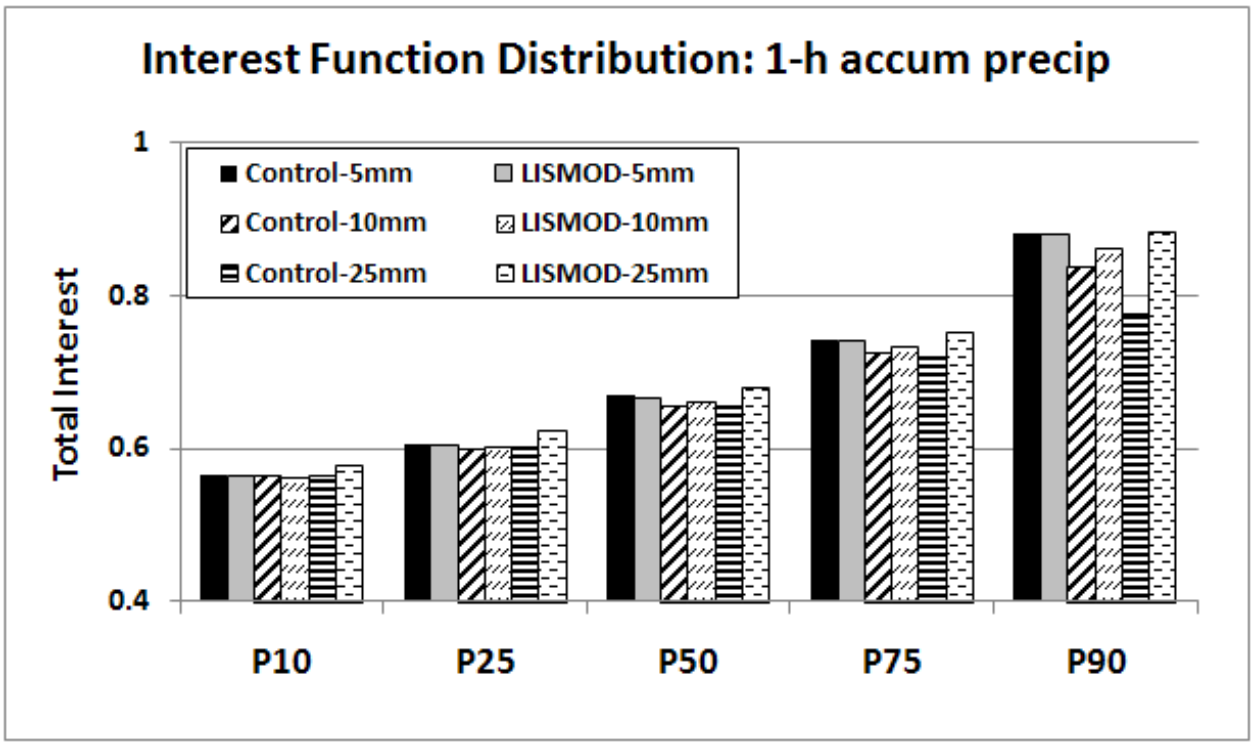

Figure 15. Distribution of the total interest function for all 81 control and LISMOD forecast/observed 1-h accumulated precipitation object pairs during the peak convective hours of 1500 to 0300 UTC. The plot depicts the control and LISMOD values within their respective interest function distributions at the 10th, 25th, 50th, 75th, and 90th percentiles for 5-mm, 10-mm, and 25-mm accumulated precipitation thresholds, according to the scale provided. The interest function sample sizes are provided in Table 6.

Table 1. A list of the LIS land surface fields and corresponding names in the WPS "METGRID.TBL" file, as used to initialize the LISMOD experimental WRF model runs.

Land Surface Field	**Name in WPS "METGRID.TBL"**
Canopy Water*	CANWAT
0-10 cm Soil Moisture	SM000010
10-40 cm Soil Moisture	SM010040
40-100 cm Soil Moisture	SM040100
100-200 cm Soil Moisture	SM100200
0-10 cm Soil Temperature	SM000010
10-40 cm Soil Temperature	SM010040
40-100 cm Soil Temperature	SM040100
100-200 cm Soil Temperature	SM100200
Skin Temperature	SKINTEMP
Snow Water Equivalent	SNOW

*Canopy water is initialized to "0" in the default WRF source code.

Table 2. A summary of the soil moisture and temperature validation statistics conducted at individual SCAN stations at the model initialization hours.

Quantity	Bias	RMS Error	Anomaly Correlation
Soil Q (5 cm) NAM	2.4 %	10.1 %	0.657
Soil Q (5 cm) LIS	0.8 %	9.2 %	0.722
Soil Q (root zone) NAM	-9.9 %	13.3 %	0.550
Soil Q (root zone) LIS	-11.7 %	14.2 %	0.557
Soil T (5 cm) NAM	-0.01 K	2.34 K	0.722
Soil T (5 cm) LIS	-0.22 K	2.53 K	0.702
Soil T (root zone) NAM	-2.01 K	2.72 K	0.783
Soil T (root zone) LIS	-2.05 K	2.91 K	0.774

Table 3. MODE Fuzzy engine weights applied to object attributes to compute "total interest" field.

Object Attribute	Weight
Centroid distance	20%
Minimum boundary distance	40%
Orientation angle difference	10%
Ratio of object areas	10%
Intersection area ratio	20%

Table 4. Comparison between the total matched and unmatched areas (in number of grid points) of the 10-mm h^{-1} precipitation objects in the control and LISMOD runs initialized at 0300 UTC 9 June 2008. The valid times span from 1800 UTC 9 June to 0300 UTC 10 June. The better (un-)matched numbers are in ***bold-italics***.

	control		**LISMOD**	
Forecast Hour	**Matched Area**	**Unmatched Area**	**Matched Area**	**Unmatched Area**
15	0	0	0	0
16	0	***78***	***100***	138
17	258	440	***270***	***332***
18	62	1 098	***380***	***704***
19	190	696	***498***	***456***
20	162	***332***	***176***	642
21	0	832	0	***464***
22	110	246	***272***	***144***
23	110	164	***194***	***154***
24	0	***156***	0	178

Table 5. Mean matched and unmatched object areas for the control and LISMOD per forecast run, and the percent improvement in LISMOD over the control. All 1-h forecasts during the peak convective hours are combined for each forecast run (12–24 h, corresponding to the 1500–0300 UTC validation window). Statistically significant differences at the 99th percentile are indicated by bold italics, while significant differences at the 90th percentile are given by italics.

Quantity	**control**	**LISMOD**	**Difference (LISMOD – control)**	**% Change**
5-mm Matched	11 911	12 045	134	1.1%
5-mm Unmatched	17 750	17 175	***-575***	***-3.2%***
10-mm Matched	2 456	2 562	*106*	*4.3%*
10-mm Unmatched	6 798	6 538	***-260***	***-3.8%***
25-mm Matched	60	60	0	0%
25-mm Unmatched	549	505	***-44***	***-8.0%***

Table 6. The number of 1-h accumulated precipitation object pairs at various thresholds composing the interest function distributions plotted in Figure 15.

	Precipitation threshold		
WRF Experiment	**5 mm**	**10 mm**	**25 mm**
control	8 934	2 479	74
LISMOD	9 077	2 445	69